

## MIT Open Access Articles

*Redox Kinetics Study of Fuel Reduced Ceria for Chemical-Looping Water Splitting*

The MIT Faculty has made this article openly available. **Please share** how this access benefits you. Your story matters.

**Citation:** Zhao, Zhenlong; Uddi, Mruthunjaya; Tsvetkov, Nikolai; Yildiz, Bilge and Ghoniem, Ahmed F. "Redox Kinetics Study of Fuel Reduced Ceria for Chemical-Looping Water Splitting." The Journal of Physical Chemistry C 120, no. 30 (August 4, 2016): 16271–16289 © 2016 American Chemical Society

**As Published:** <http://dx.doi.org/10.1021/acs.jpcc.6b01847>

**Publisher:** American Chemical Society (ACS)

**Persistent URL:** <http://hdl.handle.net/1721.1/109940>

**Version:** Author's final manuscript: final author's manuscript post peer review, without publisher's formatting or copy editing

**Terms of Use:** Article is made available in accordance with the publisher's policy and may be subject to US copyright law. Please refer to the publisher's site for terms of use.



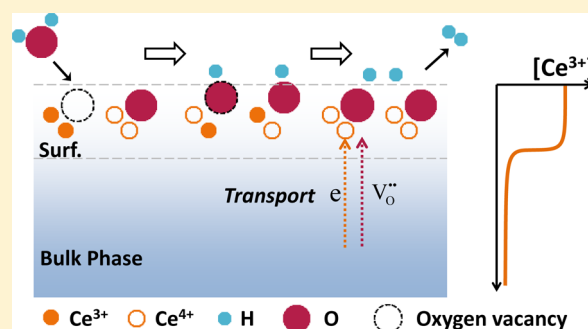
# Redox Kinetics Study of Fuel Reduced Ceria for Chemical-Looping Water Splitting

Zhenlong Zhao,<sup>†</sup> Mruthunjaya Uddi,<sup>§</sup> Nikolai Tsvetkov,<sup>‡</sup> Bilge Yildiz,<sup>\*,‡</sup> and Ahmed F. Ghoniem<sup>\*,†</sup>

<sup>†</sup>Department of Mechanical Engineering and <sup>‡</sup>Department of Nuclear Science & Engineering, Massachusetts Institute of Technology, 77 Massachusetts Avenue, Cambridge, Massachusetts 02139-4307, United States

<sup>§</sup>Department of Mechanical Engineering, University of Alabama, Tuscaloosa, Alabama 35487, United States

**ABSTRACT:** Chemical-looping water splitting is a novel and promising technology for hydrogen production with CO<sub>2</sub> separation. Its efficiency and performance depend critically on the reduction and oxidation (redox) properties of the oxygen carriers (OC). Ceria is recognized as one of the most promising OC candidates, because of its fast chemistry, high ionic diffusivity, and large oxygen storage capacity. The fundamental surface redox pathways, including the complex interactions of mobile ions and electrons between the bulk and the surface, along with the adsorbates and electrostatic fields, remain yet unresolved. This work presents a detailed redox kinetics study with emphasis on the surface ion-incorporation kinetics pathway, using time-resolved and systematic measurements in the temperature range 600–1000 °C. By using fine ceria nanopowder, we observe an order-of-magnitude higher hydrogen production rate compared to the state-of-the-art thermochemical or reactive chemical-looping water splitting studies. We show that the reduction is the rate-limiting step, and it determines the total amount of hydrogen produced in the following oxidation step. The redox kinetics is modeled using a two-step surface chemistry (an H<sub>2</sub>O adsorption/dissociation step and a charge-transfer step), coupled with the bulk-to-surface transport equilibrium. Kinetics and equilibrium parameters are extracted with excellent agreement with measurements. The model reveals that the surface defects are abundant during redox conditions, and charge transfer is the rate-determining step for H<sub>2</sub> production. The results establish a baseline for developing new materials and provide guidance for the design and the practical application of water splitting technology (e.g., the design of OC characteristics, the choice of the operating temperatures, and periods for redox steps, etc.). The method, combining well-controlled experiment and detailed kinetics modeling, enables a new and thorough approach for examining the defect thermodynamics in the bulk and at the surface, as well as redox reaction kinetics for alternative materials for water splitting.

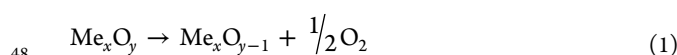


## 1. INTRODUCTION

Hydrogen is an important environmentally friendly energy carrier because of its high gravimetric energy density and zero emission. Moreover, hydrogen finds wide applications in a variety of industries, including crude oil refining, chemical production, aerospace, metal refining, food processing, and electronics manufacturing. Currently, steam methane reforming (SMR) is the major hydrogen production method. However, SMR leads to significant greenhouse gas emission, and it has already reached its maximum efficiency (70–85%).<sup>1</sup> The growing demand for clean and cost-efficient hydrogen sources has led to significant efforts to develop alternative technologies.<sup>2,3</sup>

Among a variety of options, thermochemical water splitting (TCWS) has recently attracted significant attention, because of its potential for high conversion efficiencies with limited emissions.<sup>4,5</sup> This approach is based on a two-step mechanism using a metal oxide (such as ceria-based materials) to dissociate H<sub>2</sub>O into H<sub>2</sub> and heat to reduce the metal oxide:

endothermic reduction step:



exothermic oxidation step:



The reduction step proceeds at higher temperature (above 1400 °C) to form oxygen vacancies and release O<sub>2</sub>, while the oxidation step takes place at lower temperature (below 1000 °C) to dissociate H<sub>2</sub>O and generate H<sub>2</sub>. During this process, the metal oxide transports oxygen between the two steps, remaining intact at the end of the cycle. As such, it is commonly referred to as the “oxygen carrier (OC)”. Various studies have examined different material options for TCWS, and a brief summary is presented in Table 1. Although exhibiting remarkable potentials, major challenges are related to the need for expensive high quality heat and large temperature swing which can render the process less efficient.

An immediate extension of TCWS is reactive chemical-looping water splitting (RCLWS), in which, the reduction step

Received: February 23, 2016

Revised: June 22, 2016

**Table 1. Reported Total and Peak H<sub>2</sub> Production Rates for Two-Step Thermochemical Water Splitting<sup>a</sup>**

temp (°C; red/ox)	tot H <sub>2</sub> prodn (μmol/g)	peak H <sub>2</sub> rate (μmol/g/s)	feed H <sub>2</sub> O (%)	oxygen carrier	ref
1500/800	278	6.8	44–52	CeO <sub>2</sub>	6
1500/1500	126	1.0	15	CeO <sub>2</sub> (with Rh)	7
1350/1000	32	0.15	40	CeO <sub>2</sub>	8
1500/1150	414	4.2	50, 84	CeO <sub>2</sub>	9
1350/1000	28		81	CeO <sub>2</sub>	10
1500/750	161		83	CeO <sub>2</sub> (10% Pr)	11
1400/1050	338		5.8	CeO <sub>2</sub> (25%Zr 1%Gd)	12
1300/800	109		30	Ce <sub>0.15</sub> Zr <sub>0.85</sub> O <sub>2</sub>	13
1400/1050	467.7		38.3	CeO <sub>2</sub> (50% Zr)	14, 15
1500/500	210		84	Ce <sub>0.9</sub> Hf <sub>0.1</sub> O <sub>2</sub>	16
1500/1000	153		83	CeO <sub>2</sub> (10% Mn)	17
1290/1000	62	16.4	21	CeO <sub>2</sub> (20% Zn)	18
1200/900	57		81	Ni <sub>0.5</sub> Mn <sub>0.5</sub> Fe <sub>2</sub> O <sub>4</sub>	10
1190/900	2120	9.4	56	Zn–Fe–O	19
1700/575	4270	9.1	56	FeO	20
1400/1000	195		5.8	La <sub>0.5</sub> Sr <sub>0.5</sub> MnO <sub>3</sub>	21
1350/1000	307	1.3	40	LaAlO <sub>3</sub> (with Sr, Mn)	8
1400/1000	407	5.6		La <sub>0.5</sub> Ca <sub>0.5</sub> MnO <sub>3</sub>	22

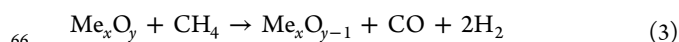
<sup>a</sup>Note some studies tested various material compositions for repeated cycles. The highest values are chosen and listed here for comparison. The conversion of the H<sub>2</sub> production unit from mL/g to μmol/g utilizes the ideal gas law at standard temperature and pressure (25 °C, 1 atm).

**Table 2. Reported Total and Peak H<sub>2</sub> Production Rates for CLWS**

temp (°C; red/ox)	tot H <sub>2</sub> prodn (μmol/g)	peak H <sub>2</sub> rate (μmol/g/s)	feed H <sub>2</sub> O (%)	oxygen carrier	reducer	ref
800/800	3460	4.8	77	Fe <sub>2</sub> O <sub>3</sub>	CH <sub>4</sub>	29
900/900	4140	8.1	30	Fe <sub>2</sub> O <sub>3</sub>	H <sub>2</sub>	30
900/900	8900	34	31	Fe <sub>2</sub> O <sub>3</sub> (with 5% CeO <sub>2</sub> )	H <sub>2</sub> +CO	31
800/800	47	0.36	5.5	Cu (with Co Pr)	H <sub>2</sub>	32
650/350	150		20	CuO	H <sub>2</sub> +CO	33
900/800	11300		20	CuFe <sub>2</sub> O <sub>4</sub>	CH <sub>4</sub>	34
900/700	12000		31	Cu <sub>0.7</sub> Fe <sub>2.3</sub> O <sub>4</sub> /Ce–ZrO <sub>2</sub>	CH <sub>4</sub>	35
900/800	2780		31	CuFe <sub>2</sub> O <sub>4</sub> /ZrO <sub>2</sub>	CH <sub>4</sub>	36
900/800	2130		31	CuFe <sub>2</sub> O <sub>4</sub> /CeO <sub>2</sub>	CH <sub>4</sub>	36
900/800	3000		47	Ni <sub>0.39</sub> Fe <sub>2.61</sub> O <sub>4</sub> (with ZrO <sub>2</sub> )	CH <sub>4</sub>	37
750/750	3500	3.8	20	WO <sub>3</sub> (with CeO <sub>2</sub> , ZrO <sub>2</sub> )	CH <sub>4</sub>	38
800/500	840	0.29	2.4	Ce <sub>0.8</sub> Zr <sub>0.2</sub> O <sub>2</sub> (with Pt)	CH <sub>4</sub>	39
850/700	500	1.1	83	CeO <sub>2</sub>	CH <sub>4</sub>	40
850/700	1580	1.3	83	Ce <sub>0.7</sub> Zr <sub>0.3</sub> O <sub>2</sub>	CH <sub>4</sub>	41
800/800	326	0.65	27	10 wt % CeO <sub>2</sub> /ZrO <sub>2</sub>	CH <sub>4</sub>	42
800/700	1020	1.0	83	CeO <sub>2</sub> (30% Fe <sub>2</sub> O <sub>3</sub> )	CH <sub>4</sub>	43
1000/1000	1240	160	26	CeO <sub>2</sub>	H <sub>2</sub>	this study
700/700	260	60	26	CeO <sub>2</sub>	H <sub>2</sub>	this study

64 is replaced by a fuel reduction reaction:

65 reduction step with fuel:



67 The utilization of fuel ensures an enhanced catalytic reaction  
 68 at lower temperature with significantly improved extent of  
 69 OC reduction and, hence, larger oxygen carrying capacity. The  
 70 required high quality heat and large temperature swing could be  
 71 replaced by an isothermal redox operation, hence leading to  
 72 a much reduced cost, enhanced stability,<sup>23–26</sup> and improved  
 73 system efficiency.<sup>27,28</sup> In contrast to TCWS, the net reaction,  
 74 combining eqs 2 and 3, is a fuel reforming reaction, where a fuel  
 75 is selectively oxidized to form hydrogen and syngas. In the case  
 76 of natural gas, the syngas stream has a H<sub>2</sub>:CO close to 2:1,  
 77 ideal for the production of H<sub>2</sub> (after shift), methanol, or liquid  
 78 fuel via Fischer–Tropsch process with CO<sub>2</sub> separation. With  
 79 the abundance and low price of natural gas, RCLWS offers a

simple and promising solution for co-producing hydrogen and  
 syngas. 80

81  
 82 Several studies have examined various metal oxide candidates  
 83 for RCLWS, including ceria, copper, ferrites, tungsten, and perov-  
 84 skites, etc. The reported H<sub>2</sub> production rates and total production  
 85 using RCLWS are summarized in Table 2. It is generally observed  
 86 that the use of ceria as an OC leads to higher H<sub>2</sub> production  
 87 because of its fast surface kinetics, high oxygen ionic diffusivity,  
 88 large oxygen carrying capacity, and robust structural stability.  
 89 The ability of ceria to accommodate high surface active site con-  
 90 centrations facilitates a relatively quick surface ion-incorporation  
 91 process.<sup>44,45</sup> The large nonstoichiometry capacity allows it to  
 92 effectively adsorb and release oxygen as it responds to the oper-  
 93 ating conditions. This property has been exploited in a large  
 94 number of applications,<sup>46,47</sup> including three-way catalyst, solid  
 95 oxide fuel cells, and electrolyzers. For the same reason, CeO<sub>2</sub> has  
 96 been suggested as a promising OC candidate for RCLWS.

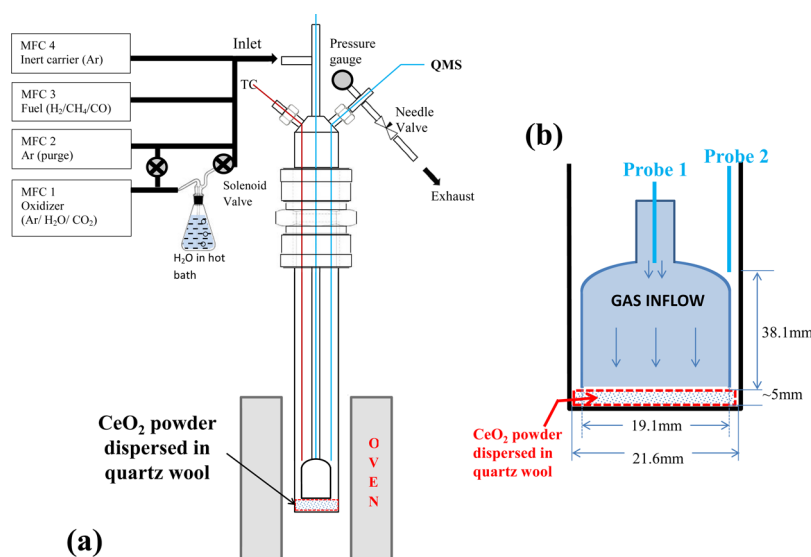


**Figure 1.** (a) Schematics of the experimental setup. (b) Schematics of the expansion tube, the sample, and the gas flow. Probe 2 is located close to the outer tube, about 1–2 mm above the top of the expansion section. Note that the  $y$ -direction of the drawing in panel b is compressed by 2.5 times as compared to  $x$ -axis for a better demonstration.

97 The bulk-phase properties of ceria-based materials have been  
 98 widely studied. The physical, chemical, and electrochemical  
 99 properties of pure and doped ceria at equilibrium have been  
 100 examined and documented.<sup>47–49</sup> Recently, there is an increas-  
 101 ing effort toward a better understanding of the surface-oriented  
 102 defect chemistry of ceria, owing to the growing interests in fuel  
 103 cells, electrolyzers, and water splitting.<sup>45,50</sup> Density functional  
 104 studies examined surface defect formation and the energy  
 105 landscape of the redox process.<sup>51–53</sup> In situ techniques, such as  
 106 in situ X-ray photoelectron spectroscopy (XPS), have emerged  
 107 recently and have been successfully applied to ceria.<sup>44,45,54–56</sup>  
 108 The majority of the work concentrated on the surface and  
 109 intermediate species at equilibrium. Despite the recent efforts  
 110 in developing analytical models for reaction kinetics,<sup>57–60</sup> the  
 111 fundamental surface redox pathway of ceria is not well under-  
 112 stood. The complexities involved in the interactions of mobile  
 113 ions, and electrons between the bulk and the surface, along with  
 114 the adsorbates and electrostatic fields remain yet unresolved.  
 115 Applying ceria in RCLWS requires a good knowledge of  
 116 the time-resolved reactivity under conditions relevant for its  
 117 application (temperature and gaseous composition), which is  
 118 still missing.

119 In this work, we investigate the ceria redox mechanism with  
 120 an emphasis on the surface ion-incorporation kinetics pathway,  
 121 using a detailed time-resolved measurement under conditions  
 122 relevant for RCLWS. Isothermal redox cycles of CeO<sub>2</sub> nano-  
 123 powder are carried out in a button cell reactor in the tempera-  
 124 ture range 600–1000 °C. H<sub>2</sub> is used as a surrogate fuel in this  
 125 study in order to explore the fundamentals of redox reactions  
 126 on ceria. The reaction kinetics is determined by quantifying  
 127 the flue stream composition using an online quadrupole mass  
 128 spectrometer (QMS). H<sub>2</sub> is produced by water splitting during  
 129 the oxidation cycle as a mixture of H<sub>2</sub>O vapor and Ar is flown  
 130 over CeO<sub>2</sub> samples. An order-of-magnitude higher hydrogen  
 131 production rate is observed as compared to the state-of-the-art  
 132 TCWS (Table 1) and RCLWS (Table 2) methods, resulting  
 133 from the utilization of fine ceria nanopowder, which also ensures  
 134 a surface-reaction-limited process. Kinetic models are subse-  
 135 quently developed to characterize the oxygen-ion-incorporation  
 136 dynamics during the redox process. The model consists of a

series of intermediate steps: adsorption/dissociation of gaseous  
 reactant, charge transfer on the surface, and the bulk-to-surface  
 transport. The model reveals the importance of the surface defect  
 and its connection to the bulk phase. Driven by the difference of  
 the defect formation energy, the surface is enriched with the key  
 defects (oxygen vacancy and polarons), consistent with the in situ  
 observations reported in the literature.<sup>44,45</sup> With the proposed  
 kinetics, the rate-limiting step is identified, and suggestions are  
 obtained for the development of better materials in the future.

## 2. EXPERIMENT

The experimental setup consists of a gas delivery system,  
 a control unit, a central quartz reactor tube, and a real time  
 flue gas analysis system with an online mass spectrometer.  
 The system layout and the details of the reactor are shown in  
 Figure 1.<sup>61</sup> Four Brooks GF40 MultiFlo digital thermal mass  
 flow controllers (MFCs) are used for the gas flow control. The  
 reactor is made of a quartz tube positioned inside an ATS 3210  
 split tube furnace that provides an isothermal environment  
 up to 1100 °C. As shown in Figure 1b, the reactor consists of  
 an outer tube (305 mm length, 25.4 mm outer diameter (o.d.),  
 and 21.6 mm inner diameter (i.d.)), and an inner concentric  
 6.4 mm o.d. quartz tube with an expanding section of 19.1 mm  
 o.d., 38.1 mm length. Gases flow through the central tube,  
 impinge on the bottom of the outer tube, and exit reversely  
 through the exhaust. Capillary probes made of quartz (0.53 mm  
 i.d., 0.80 mm o.d.) are used to sample minute amounts of gases,  
 before and after reactions. The probe sampling the exhaust flow  
 is located close to the outer tube, around 1–2 mm above the  
 top of the expansion section of the inner tube. A quadrupole  
 mass spectrometer (HPR20 from Hiden Analytical Inc.) is used  
 to analyze the flue gas composition. The QMS has a response  
 time of less than 300 ms and a wide bandwidth of species detec-  
 tion capability.

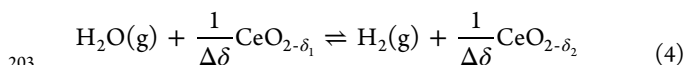
Ceria powder from Sigma-Aldrich (99.95% purity) is used for  
 the reaction study. Table 3 lists the properties of the sample.  
 The BET surface area is 15.4 m<sup>2</sup>/g, and the average size of the  
 particle is 50 nm. A 100 mg amount of ceria powder is embed-  
 ded in quartz wool and placed at the bottom of the outer quartz tube.

Table 3. Some Physical Properties of the CeO<sub>2</sub>

property	value (unit)
density, $\rho$	7.22 g cm <sup>-3</sup>
molar density, $\tilde{\rho}_{\text{Ce}}$	4.19 × 10 <sup>4</sup> mol m <sup>-3</sup>
lattice constant, $a$	0.54112 nm
surface molar density, $\tilde{\rho}_{\text{Ce},s} = \tilde{\rho}_{\text{Ce}}a$	2.27 × 10 <sup>-5</sup> mol m <sup>-2</sup>
melting point	2750 K
relative dielectric constant (0.5–50 MHz)	11
fresh sample	
bulk density	0.53 g cm <sup>-3</sup>
purity	99.95%
specific surface area, $s_0$	15.4 m <sup>2</sup> g <sup>-1</sup>
particle size	~50 nm
cycled sample	
specific surface area, $s_1$	3.99 m <sup>2</sup> g <sup>-1</sup>
particle size	~200 nm

174 A lesser amount of sample is also tested (50 and 25 mg), and  
 175 negligible difference is found in the obtained redox kinetics.  
 176 The sample undergoes redox cycles, with argon as purging gas  
 177 flowing in between. Oxidation is performed using a gas mixture  
 178 of water vapor and argon. Ar is slowly bubbled through a 1 gallon  
 179 bottle filled with deionized water maintained at 80 ± 0.5 °C in  
 180 an insulated heat bath to prepare the oxidizing mixture. The  
 181 steam mixture is further diluted with Ar to achieve the desirable  
 182 H<sub>2</sub>O concentration. The total flow rate into the reactor during  
 183 the oxidation step is maintained constant at 337 cm<sup>3</sup>(STP)/min,  
 184 and the H<sub>2</sub>O mole fraction is varied between 5% and 26%.  
 185 H<sub>2</sub>–Ar mixture is used for the reduction, with the total flow fixed  
 186 at 350 cm<sup>3</sup>(STP)/min and the H<sub>2</sub> mole fraction from 5% to  
 187 20%. While the ultimate technology objective is to use methane  
 188 for reduction, H<sub>2</sub> is used as a surrogate to examine the process  
 189 while simplifying the modeling of the redox reactions. All con-  
 190 necting stainless steel tubes are heated above 140 °C to avoid  
 191 water condensation. The oxidation and reduction times are  
 192 fixed at 2 min each for the base case. Before measurements, the  
 193 samples are pretreated for 100 redox cycles at 1000 °C to reach  
 194 periodic stationary states. Afterward, the measurements are taken  
 195 from 1000 °C until 600 °C with a step of 50 °C. Each operating  
 196 condition is repeated for at least five times, and results are  
 197 averaged to reduce the noise. The measurements at 500 °C are  
 198 also taken as a reference, although the reactivity is too low and  
 199 can hardly be distinguished from background noise. Experiments  
 200 with different oxidation and reduction conditions are also carried  
 201 out to evaluate the effects on the H<sub>2</sub> production reactivity.

202 The redox process can be written as a reversible reaction:



204 where  $\Delta\delta = \delta_1 - \delta_2$  is the bulk-phase nonstoichiometry change.  
 205 In order to derive the H<sub>2</sub> production rate based on the flue  
 206 stream composition, we consider a control volume as out-  
 207 lined in Figure 1b. In the redox process, the production  
 208 (or consumption) of 1 mol of H<sub>2</sub>O leads to the consumption  
 209 (or production) of 1 mol of H<sub>2</sub>. Therefore, the total molar  
 210 flow rate throughout the control volume remains constant; i.e.,  
 211  $\dot{n}_{\text{in}} = \dot{n}_{\text{out}}$ . Thus, we can express the reaction rates as

212 oxidation:

$$213 \quad \omega_{\text{H}_2} = \frac{X_{\text{H}_2,\text{out}} \dot{n}_{\text{ox},\text{out}}}{m_{\text{CeO}_2}} = \frac{X_{\text{H}_2,\text{out}} P^0 \dot{V}_{\text{ox},\text{in}}^0}{m_{\text{CeO}_2} RT^0} \quad (5)$$

reduction:

$$\omega_{\text{H}_2\text{O}} = \frac{X_{\text{H}_2\text{O},\text{out}} \dot{n}_{\text{red},\text{out}}}{m_{\text{CeO}_2}} = \frac{X_{\text{H}_2\text{O},\text{out}} P^0 \dot{V}_{\text{red},\text{in}}^0}{m_{\text{CeO}_2} RT^0} \quad (6) \quad 214$$

215  $X_{\text{H}_2,\text{out}}$  and  $X_{\text{H}_2\text{O},\text{out}}$  are the measured mole fractions of the  
 216 produced H<sub>2</sub> and H<sub>2</sub>O at the exit.  $\dot{n}_{\text{ox},\text{in}}$  and  $\dot{n}_{\text{red},\text{in}}$  are the total  
 217 molar inflow rates of the gas mixture for the oxidation and  
 218 reduction, respectively.  $P^0$ ,  $T^0$ , and  $V^0$  are the pressure, tempera-  
 219 ture, and the total volumetric inflow rate at standard tempera-  
 220 ture and pressure (STP). The reaction rates (unit,  $\mu\text{mol g}^{-1}\text{s}^{-1}$ )  
 221 are normalized by the total ceria sample  $m_{\text{CeO}_2}$ , i.e., 100 mg,  
 222 used in the measurement. The derivation assumes a quasi-  
 223 steady state and neglects the accumulation or depletion effect in  
 224 the control volume. This is valid as the flow residence time is  
 225 much shorter ( $\sim 0.1$  s) than the characteristic time of the redox  
 226 conversion.<sup>61</sup>  $\Delta\delta$  is calculated as  
 227

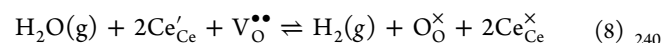
$$|\Delta\delta(t)| = n_{\text{O}}(t)/n_{\text{CeO}_2} \quad (7) \quad 228$$

229 where  $n_{\text{O}}(t) = \int_0^t \dot{\omega}_{\text{H}_2} dt$  is the accumulated intake of oxygen  
 230 ions.  $n_{\text{CeO}_2} = m_{\text{CeO}_2}/M_{\text{CeO}_2}$  is the moles of ceria used in the  
 231 experiment.  $M_{\text{CeO}_2}$  is the molecular weight.

### 3. THEORY

232 To model the reaction kinetics, ceria particles at cyclic stationary  
 233 state are treated as identical spheres with diameter  $r_p = 100$  nm  
 234 (Table 3). The particle size is assumed to remain unchanged  
 235 during the redox cycle, as CeO<sub>2</sub> is known to maintain its  
 236 fluorite structure even under large nonstoichiometry at elevated  
 237 temperatures.<sup>47</sup>

238 The overall reaction between the bulk ceria and the external  
 239 gas-phase reactants may be written as<sup>47–49</sup>



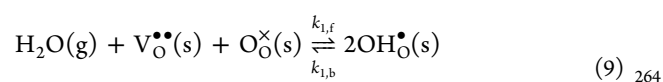
241 where  $\text{V}_{\text{O}}^{\bullet\bullet}$  is a doubly charged oxygen vacancy,  $\text{O}_{\text{O}}^{\times}$  is an oxygen  
 242 ion on a normal site.  $\text{Ce}'_{\text{Ce}}$  denotes a polaron (a localized  
 243 electron,  $\text{Ce}^{3+}$ ), and  $\text{Ce}^{\times}_{\text{Ce}}$  is a regular  $\text{Ce}^{4+}$  cation.  $\text{Ce}'_{\text{Ce}}$  and  $\text{V}_{\text{O}}^{\bullet\bullet}$   
 244 are believed to be the major defects in the bulk as well as on the  
 245 surface.<sup>44,47–49</sup>

246 Equation 8 merely describes the overall equilibrium between  
 247 the defects in the bulk ceria and oxygen from the H<sub>2</sub>O/H<sub>2</sub>  
 248 environment. The electrochemical process, however, involves  
 249 serial steps of important heterogeneous surface reactions, i.e.,  
 250 adsorption/dissociation of gaseous reactant forming adsorbates,  
 251 ion/electron transfer on the surface, and association and desorp-  
 252 tion of products. The surface chemistry is further connected  
 253 with the bulk phase via bulk-to-surface transport driven by  
 254 the electrochemical potential gradient. Bulk-phase diffusion con-  
 255 tinues to adjust the spatial defect distribution and eventually  
 256 equilibrates the sample with the environment. Figure 2 schemati-  
 257 cally highlights the key steps in the oxidation direction.

258 In the following two subsections, we will present the submodels  
 259 for the surface chemistry and diffusion process, respectively.

260 **Surface Chemistry.** The surface water splitting and oxygen-  
 261 incorporation reactions are modeled using a two-step mecha-  
 262 nism (Figure 2a):<sup>45,50–53</sup>

263 R1:



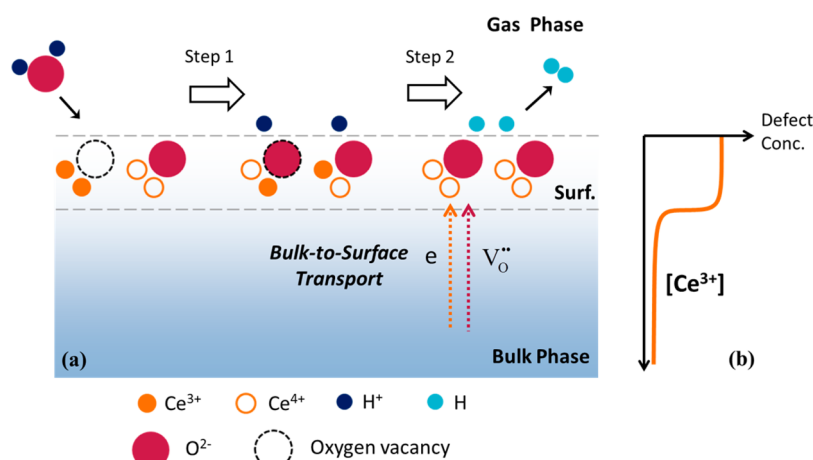
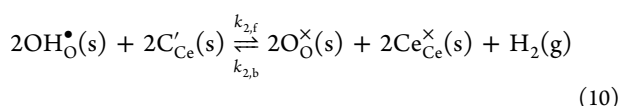


**Figure 2.** (a) Schematics of the water splitting pathway. The ion-incorporation surface process comprises the adsorption and dissociation of H<sub>2</sub>O forming OH<sup>•</sup> (R1) and charge transfer, association, and desorption of H<sub>2</sub> (R2). The heterogeneous chemistry is linked to bulk phase via the bulk-to-surface transport of the electron defect,  $e$ , and the oxygen vacancy defect,  $V_{\text{O}}^{\bullet\bullet}$ . (b) Schematics of the surface enrichment of Ce<sup>3+</sup> relative to the bulk.

265 R2:



266

267 OH<sup>•</sup><sub>O</sub> is a hydroxyl ion group on an oxygen anion site. The  
268 surface reactions are assumed to occur only within the first unit  
269 cell layer on the surface, and s in the parentheses emphasizes  
270 this assumption. R1 describes the adsorption and dissociation  
271 process: a H<sub>2</sub>O molecule is adsorbed onto an oxygen vacancy  
272 site and dissociates into a hydroxyl ion and an extra proton,  
273 which then bonds to an adjacent oxygen to form a second OH<sup>•</sup><sub>O</sub>  
274 group. R2 describes the charge-transfer process, followed by the  
275 association and desorption of H<sub>2</sub>.

276 Using the law of mass action, we express the species reaction  
277 rates for R1 and R2 as

$$r_1 = k_{1,\text{f}}p_{\text{H}_2\text{O}}[V_{\text{O}}^{\bullet\bullet}]_{\text{s}}[O_{\text{O}}^{\times}]_{\text{s}} - k_{1,\text{b}}[\text{OH}_{\text{O}}^{\bullet}]_{\text{s}}^2 \quad (11)$$

278

$$r_2 = k_{2,\text{f}}[\text{OH}_{\text{O}}^{\bullet}]_{\text{s}}^2[\text{Ce}'_{\text{Ce}}]_{\text{s}}^2 - k_{2,\text{b}}p_{\text{H}_2}[O_{\text{O}}^{\times}]_{\text{s}}^2[\text{Ce}^{\times}_{\text{Ce}}]_{\text{s}}^2 \quad (12)$$

279

280 In eqs 11 and 12, the brackets denote the mole of species  
281 per mole of CeO<sub>2</sub>. The subscript, s, again, emphasizes that the  
282 concentrations of the reactant are taken on the surface.  $k_{i,\text{f}}$  and  
283  $k_{i,\text{b}}$  denote the rate coefficients (unit, s<sup>-1</sup>) of the aforemen-  
284 tioned reactions and are assumed to follow the Arrhenius  
285 expression. Partial pressure of H<sub>2</sub> or H<sub>2</sub>O in the gas phase is  
286 defined with respect to the reference value (i.e., 1 atm). Because  
287 of the high flow rates used in this study, the gas residence  
288 time through the control volume (Figure 1b) is much shorter  
289 (<300 ms) as compared to chemistry, and thus the reactant  
290 partial pressure on the surface is essentially identical to that in  
291 the gas phase as measured in the QMS. Therefore, the measured  
292  $p_{\text{H}_2\text{O}}$  and  $p_{\text{H}_2}$  accurately represent the redox environment to  
293 which the ceria sample is exposed. At equilibrium,  $r_1$  and  $r_2$   
294 are zero. This leads to the definition of the corresponding  
295 equilibrium constants  $K_1$  and  $K_2$ .

296 A similar pathway has been discussed in the literature.<sup>45,50–53</sup>  
297 Feng et al.<sup>45</sup> emphasized the importance of the charge-  
298 transfer process, by further breaking R2 into OH<sup>•</sup><sub>O</sub> + Ce'<sub>Ce</sub> →  
299 OH<sup>•</sup><sub>O</sub> + Ce'<sub>Ce</sub>, followed by the dissociation 2OH<sup>•</sup><sub>O</sub> = 2O<sup>•</sup><sub>O</sub> +  
300 H<sub>2</sub>(g). Similar steps were calculated in a theoretical study by

Marrocchelli and Yildiz.<sup>51</sup> Hansen and Wolverton<sup>52</sup> calculated  
301 the minimum energy pathway during R2 and concluded that  
302 the process may happen asymmetrically: Ce<sup>3+</sup> hops close to  
303 OH<sup>•</sup><sub>O</sub> and weakens the O–H bond; the weakly bonded proton  
304 then moves toward the adjacent OH<sup>•</sup><sub>O</sub> and forms H<sub>2</sub> as the  
305 last Ce<sup>3+</sup> is oxidized. Identifying the detailed elementary steps  
306 during R2 is beyond the scope of this study. Here we couple  
307 the charge transfer with the H<sub>2</sub> formation process and model it  
308 as a single step. 309

The governing equations for the surface species are written as 310

$$\frac{\partial \tilde{C}_i}{\partial t} = \dot{R}_i + \dot{J}_i \quad i = \text{OH}_{\text{O}}^{\bullet}, V_{\text{O}}^{\bullet\bullet} \quad (13) \quad 311$$

where  $\tilde{C}_i$  is the species concentration on the surface,  $\dot{R}_i$  is the  
312 production/consumption rate of species  $i$ , and  $\dot{J}_i$  is the diffusion  
313 flux from the bulk phase. We proceed by coupling these species  
314 equations with the O- and Ce-site conservation equations and  
315 the electroneutrality condition: 316

O-site: 317

$$[V_{\text{O}}^{\bullet\bullet}]_{\text{s}} + [\text{OH}_{\text{O}}^{\bullet}]_{\text{s}} + [O_{\text{O}}^{\times}]_{\text{s}} = 2 \quad (14) \quad 318$$

Ce-site: 319

$$[\text{Ce}'_{\text{Ce}}]_{\text{s}} + [\text{Ce}^{\times}_{\text{Ce}}]_{\text{s}} = 1 \quad (15) \quad 320$$

electroneutrality: 321

$$2[V_{\text{O}}^{\bullet\bullet}]_{\text{s}} + [\text{OH}_{\text{O}}^{\bullet}]_{\text{s}} = [\text{Ce}'_{\text{Ce}}]_{\text{s}} \quad (16) \quad 322$$

It is worth noting that the electroneutrality condition may  
323 break down in the space-charge region (SC) on the surface.  
324 The doubly charged oxygen vacancies along with the polarons  
325 form a double layer (i.e., positive charge from V<sup>••</sup><sub>O</sub> on one  
326 layer and negative charge from Ce'<sub>Ce</sub> on the other), creating a  
327 large disturbance of the spatial electrostatic potential gradient  
328 near the surface. This may lead to charge enrichment and  
329 simultaneous countercharge depletion in this region. However,  
330 Chueh and co-workers reported surface enrichment for both  
331 V<sup>••</sup><sub>O</sub><sup>45</sup> and Ce'<sub>Ce</sub><sup>44</sup> in SC for Sm-doped CeO<sub>2</sub>. Feng et al.<sup>45</sup>  
332 further quantified the contribution of the electrostatic potential  
333 gradient near the surface under redox conditions and concluded  
334 that the charge neutrality is preserved near the surface. As such,  
335 we adopt the electroneutrality assumption in this study for the 336

337 sake of simplicity. This assumption can be relaxed and examined  
338 in depth in future study.

339 With eqs 14–16, the two species equations ( $\text{OH}_{\text{O}}^{\bullet}$ ,  $\text{V}_{\text{O}}^{\bullet\bullet}$ )  
340 describe the surface kinetics. Since the proton conductivity is  
341 less pronounced compared to the major defects (vacancies  
342 and polarons) in the bulk, we assume that all hydroxyl ions  
343 are confined to the surface layer and hence neglect its diffusion.  
344 Thus, we express the species conservation equations for the  
345 surface hydroxyl group and the surface oxygen vacancy as

$$346 \quad \tilde{\rho}_{\text{Ce},s} \frac{\partial [\text{OH}_{\text{O}}^{\bullet}]_s}{\partial t} = \tilde{\rho}_{\text{Ce},s} (2r_1 - 2r_2) \quad (17)$$

$$347 \quad \tilde{\rho}_{\text{Ce},s} \frac{d[\text{V}_{\text{O}}^{\bullet\bullet}]_s}{dt} = -\tilde{\rho}_{\text{Ce},s} r_1 + \dot{J}_{\text{V}_{\text{O}}^{\bullet\bullet}} \quad (18)$$

348 Here  $\tilde{\rho}_{\text{Ce},s}$  is the surface molar density of the unit cell (unit,  
349  $\text{mol m}^{-2}$ ). With the knowledge of  $\dot{J}_{\text{V}_{\text{O}}^{\bullet\bullet}}$ , eqs 17 and 18 complete  
350 the description of the surface species evolution under the redox  
351 conditions.

352 **Bulk-to-Surface Transport.** The conservation of a defect  
353 species  $i$  can be expressed as

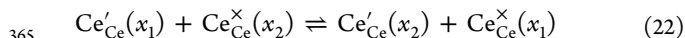
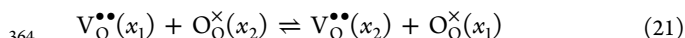
$$354 \quad \frac{\partial C_i}{\partial t} + \frac{1}{r^2} \frac{\partial}{\partial r} (r^2 \dot{J}_i) = 0 \quad i = \text{V}_{\text{O}}^{\bullet\bullet}, \text{Ce}'_{\text{Ce}} \quad (19)$$

355 where  $C_i$  is the molar concentration and  $\dot{J}_i$  the flux of the defect  
356 species  $i$ . In eq 19, we assume a 1D spherically symmetric  
357 diffusion. The flux density is expressed using the Nernst–Planck  
358 equation:

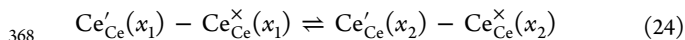
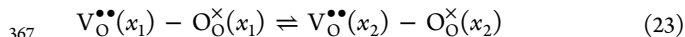
$$359 \quad \dot{J}_i = -\frac{C_i D_i}{RT} \frac{\partial \tilde{\mu}_i^*}{\partial r} \quad (20)$$

360 where  $D_i$  is the diffusion coefficient,  $R$  the universal gas constant,  
361 and  $T$  the temperature.  $\tilde{\mu}_i^*$  is the electrochemical potential.

362 The diffusion process involves the exchange of defects between  
363 two points,  $x_1$  and  $x_2$ :<sup>62</sup>



366 By rearranging the above equations, we obtain equivalently



369 Equations 23 and 24 restate the diffusion process in terms of the  
370 “defect elements”, i.e., the structural defect minus the original  
371 normal site.<sup>62</sup> Thus,  $\tilde{\mu}_i^*$  for the oxygen vacancy and polaron can  
372 be expressed as

$$373 \quad \tilde{\mu}_{\text{V}_{\text{O}}^{\bullet\bullet}}^* = \tilde{\mu}_{\text{V}_{\text{O}}^{\bullet\bullet}} - \tilde{\mu}_{\text{O}_{\text{O}}^{\times}} \quad (25)$$

$$374 \quad \tilde{\mu}_{\text{Ce}'_{\text{Ce}}}^* = \tilde{\mu}_{\text{Ce}'_{\text{Ce}}} - \tilde{\mu}_{\text{Ce}_{\text{Ce}}^{\times}} \quad (26)$$

375 Here  $\tilde{\mu}_i$  is the electrochemical potential for each species. We  
376 note that the contribution of the normal sites ( $\tilde{\mu}_{\text{O}_{\text{O}}^{\times}}$  and  $\tilde{\mu}_{\text{Ce}_{\text{Ce}}^{\times}}$ )  
377 to the diffusion process cannot be neglected here, because the  
378 redox conversion involves a large nonstoichiometry change, and  
379 the availability of the normal sites significantly influences the  
380 diffusion.

381 We proceed by defining the electrochemical potential of the  
382 structural defects and the normal sites as

$$383 \quad \tilde{\mu}_j = \mu_j^0 + RT \ln a_j + z_j F \phi \quad j = \text{V}_{\text{O}}^{\bullet\bullet}, \text{O}_{\text{O}}^{\times}, \text{Ce}'_{\text{Ce}}, \text{Ce}_{\text{Ce}}^{\times} \quad (27)$$

where  $\mu_j^0$  is the chemical potential at the reference condition 384  
and  $z_j$  the effective charge.  $\phi$  is the internal electrostatic 385  
potential.  $F$  is the Faraday constant.  $a_j$  is the activity, defined as 386

$$a_j = \gamma_j \frac{C_j}{C_{\text{ref}}} \quad (28) \quad 387$$

where  $\gamma_j$  is the activity coefficient and  $C_{\text{ref}} = \text{constant}$  is a 388  
reference molar concentration. Assuming that  $\gamma_j$  is independent 389  
of concentration, we express the spatial derivatives of  $\tilde{\mu}_j$  as 390

$$\frac{\partial \tilde{\mu}_j}{\partial r} = \frac{\partial \mu_j^0}{\partial r} + RT \frac{\partial \ln C_j}{\partial r} + z_j F \frac{\partial \phi}{\partial r} \quad (29) \quad 391$$

Substituting eqs 25–29 into eq 19 yields 392

$$\begin{aligned} \frac{\partial [\text{V}_{\text{O}}^{\bullet\bullet}]}{\partial t} = \frac{1}{r^2} \frac{\partial}{\partial r} \left\{ \frac{r^2 [\text{V}_{\text{O}}^{\bullet\bullet}] D_{\text{V}_{\text{O}}^{\bullet\bullet}}}{RT} \left[ \frac{\partial (\mu_{\text{V}_{\text{O}}^{\bullet\bullet}}^0 - \mu_{\text{O}_{\text{O}}^{\times}}^0)}{\partial r} \right. \right. \\ \left. \left. + RT \frac{\partial}{\partial r} \ln \left( \frac{[\text{V}_{\text{O}}^{\bullet\bullet}]}{[\text{O}_{\text{O}}^{\times}]} \right) + 2F \frac{\partial \phi}{\partial r} \right] \right\} \end{aligned} \quad (30) \quad 393$$

$$\begin{aligned} \frac{\partial [\text{Ce}'_{\text{Ce}}]}{\partial t} = \frac{1}{r^2} \frac{\partial}{\partial r} \left\{ \frac{r^2 [\text{Ce}'_{\text{Ce}}] D_{\text{Ce}'_{\text{Ce}}}}{RT} \left[ \frac{\partial (\mu_{\text{Ce}'_{\text{Ce}}}^0 - \mu_{\text{Ce}_{\text{Ce}}^{\times}}^0)}{\partial r} \right. \right. \\ \left. \left. + RT \frac{\partial}{\partial r} \ln \left( \frac{[\text{Ce}'_{\text{Ce}}]}{[\text{Ce}_{\text{Ce}}^{\times}]} \right) - F \frac{\partial \phi}{\partial r} \right] \right\} \end{aligned} \quad (31) \quad 394$$

Coupling with the Ce- and O-site conservation equations and 395  
the electroneutrality condition: 396

O-site: 397

$$[\text{V}_{\text{O}}^{\bullet\bullet}] + [\text{O}_{\text{O}}^{\times}] = 2 \quad (32) \quad 398$$

Ce-site: 399

$$[\text{Ce}'_{\text{Ce}}] + [\text{Ce}_{\text{Ce}}^{\times}] = 1 \quad (33) \quad 400$$

electroneutrality: 401

$$2[\text{V}_{\text{O}}^{\bullet\bullet}] = [\text{Ce}'_{\text{Ce}}] \quad (34) \quad 402$$

Equations 30–34 formulate a complete description of the bulk 403  
diffusion process. 404

The characteristics and the properties of the ceria sample 405  
allow us to significantly simplify these equations. The electronic 406  
and ionic diffusivities ( $D_{\text{Ce}'_{\text{Ce}}}$ ,  $D_{\text{V}_{\text{O}}^{\bullet\bullet}}$ ) of ceria are very high 407  
and bring the bulk defects to dynamic equilibrium during the 408  
redox process. Using the diffusivity data reported in ref 63, 409  
the characteristic time,  $t$ , for a diffusion-limited process from 410  
the expression  $t \sim R^2/4D$ , is estimated to be less than 200 ms, 411  
which is significantly faster compared to the surface chemistry. 412  
A more rigorous calculation that takes into account the temporal 413  
and spatial variation of the defect concentration is included in 414  
Appendix A, which shows that the concentration variation caused 415  
by the mass-transfer resistance is less than 4%. This estimation 416  
indicates that the bulk diffusion within the ceria macroparticle 417  
is fast enough that any spatial variations of  $\tilde{\mu}_{\text{V}_{\text{O}}^{\bullet\bullet}}^*$  and  $\tilde{\mu}_{\text{Ce}'_{\text{Ce}}}^*$  will be 418  
readily removed via diffusion. As such, the conversion process is 419  
essentially surface-reaction-limited. Thus,  $\tilde{\mu}_{\text{V}_{\text{O}}^{\bullet\bullet}}^*$  and  $\tilde{\mu}_{\text{Ce}'_{\text{Ce}}}^*$  remain 420  
uniform throughout the particle while responding dynamically 421

422 to the changing environment. Equations 30 and 31 can be  
423 simplified as

424  $\tilde{\mu}_{V_{O}^{\bullet\bullet}}^* = \text{constant}$ :

$$425 \frac{\partial}{\partial r}(\mu_{V_{O}^{\bullet\bullet}}^0 - \mu_{O_{O}^{\times}}^0) + RT \frac{\partial}{\partial r} \ln \left( \frac{[V_{O}^{\bullet\bullet}]}{[O_{O}^{\times}]} \right) + 2F \frac{\partial \phi}{\partial r} = 0 \quad (35)$$

426  $\tilde{\mu}_{Ce'_{Ce}}^* = \text{constant}$ :

$$427 \frac{\partial}{\partial r}(\mu_{Ce'_{Ce}}^0 - \mu_{Ce_{Ce}^{\times}}^0) + RT \frac{\partial}{\partial r} \ln \left( \frac{[Ce'_{Ce}]}{[Ce_{Ce}^{\times}]} \right) - F \frac{\partial \phi}{\partial r} = 0 \quad (36)$$

428 However, the uniformity of the  $\tilde{\mu}_{V_{O}^{\bullet\bullet}}^*$  and  $\tilde{\mu}_{Ce'_{Ce}}^*$  does not  
429 necessarily mean the same value of the defect concentration,  
430  $V_{O}^{\bullet\bullet}$  and  $Ce'_{Ce}$  in the bulk and at the surface. In fact, owing to  
431 the difference of the standard chemical potentials ( $\mu_{V_{O}^{\bullet\bullet}}^0 - \mu_{O_{O}^{\times}}^0$   
432 and  $\mu_{Ce'_{Ce}}^0 - \mu_{Ce_{Ce}^{\times}}^0$ ) between the bulk and the surface, a pro-  
433 nounced surface defect segregation phenomenon (see schematics  
434 in Figure 2b) has been observed in several studies.<sup>44,45,55</sup> Chueh  
435 et al.<sup>44</sup> reported a two-order-of-magnitude surface-to-bulk  $Ce'_{Ce}$   
436 enrichment for Sm-doped ceria at 466 °C. Similar results were  
437 observed for the oxygen vacancies by Feng et al.<sup>45</sup> To model the  
438 surface effect, we assume that  $\mu_j^0$  varies from the bulk ( $r < r_p$ ) to  
439 the surface ( $r = r_p$ ) according to a step function, as depicted in  
440 Figure 3. Thus, the defect concentration in the bulk phase is

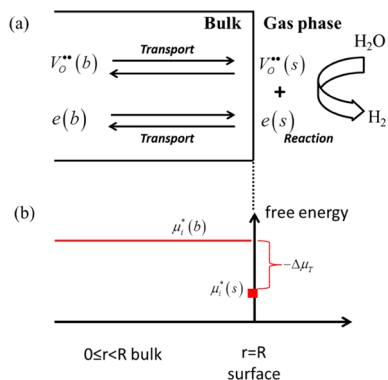


Figure 3. Schematics of (a) the bulk-to-surface transport model and (b) the difference of the defect formation energy. b and s in parentheses denote the defects in the bulk phase and on the surface, respectively.

441 uniform, and it connects dynamically to the kinetic process on  
442 the surface via diffusion. Eliminating  $\phi$  in eqs 35 and 36 and  
443 integrating from the bulk to the surface yield

$$444 \frac{[V_{O}^{\bullet\bullet}]_s [Ce'_{Ce}]_s^2 / [O_{O}^{\times}]_s [Ce_{Ce}^{\times}]_s^2}{[V_{O}^{\bullet\bullet}]_b [Ce'_{Ce}]_b^2 / [O_{O}^{\times}]_b [Ce_{Ce}^{\times}]_b^2} = \exp \left( -\frac{\Delta \mu_T^0}{RT} \right) = K_T \quad (37)$$

445 where

$$446 \Delta \mu_T^0 = (\mu_{V_{O}^{\bullet\bullet}}^0 - \mu_{O_{O}^{\times}}^0 + 2\mu_{Ce'_{Ce}}^0 - 2\mu_{Ce_{Ce}^{\times}}^0)_{\text{surface}} - (\mu_{V_{O}^{\bullet\bullet}}^0 - \mu_{O_{O}^{\times}}^0 + 2\mu_{Ce'_{Ce}}^0 - 2\mu_{Ce_{Ce}^{\times}}^0)_{\text{bulk}} \quad (38)$$

447 Equation 37 essentially describes the transport equilibrium between  
448 the bulk and the surface, by combining reactions 23 and 24, as

$$V_{O}^{\bullet\bullet}(b) - O_{O}^{\times}(b) + 2Ce'_{Ce}(b) - 2Ce_{Ce}^{\times}(b) \\ \Rightarrow V_{O}^{\bullet\bullet}(s) - O_{O}^{\times}(s) + 2Ce'_{Ce}(s) - 2Ce_{Ce}^{\times}(s) \quad (39) \quad 449$$

If we add  $1/2 O_2$  to both sides of eq 39, we arrive at the defect  
450 formation reaction:<sup>47–49</sup> 451

$$O_{O}^{\times}(b) + 2Ce_{Ce}^{\times}(b) \Rightarrow V_{O}^{\bullet\bullet}(b) + 2Ce'_{Ce}(b) + 1/2 O_2 \quad (40) \quad 452$$

$$O_{O}^{\times}(s) + 2Ce_{Ce}^{\times}(s) \Rightarrow V_{O}^{\bullet\bullet}(s) + 2Ce'_{Ce}(s) + 1/2 O_2 \quad (41) \quad 453$$

for the bulk and the surface, respectively. Therefore,  $\Delta \mu_T^0$  is the  
454 difference in the formation energy of the defect between the  
455 surface (eq 41) and the bulk phase (eq 40),  $\Delta \mu_T^0 = \Delta \mu_{R,s}^0 -$   
456  $\Delta \mu_{R,b}^0$ , where  $\Delta \mu_{R,b}^0$  and  $\Delta \mu_{R,s}^0$  are the Gibbs free energy of  
457 reaction for eqs 40 and (41), respectively.  $\Delta \mu_T^0$  can be further  
458 related to  $\Delta h_T^0$  and  $\Delta s_T^0$ , as 459

$$\Delta \mu_T^0 = \Delta h_T^0 - T \Delta s_T^0 \quad (42) \quad 460$$

Creation of one defect involves breaking up four Ce–O bonds  
461 in the bulk, but fewer on the surface. Thus, defects are more  
462 energetically favored on the surface. On the other hand, the  
463 defect formation causes the relaxation of the adjacent atoms  
464 with reduced vibrational frequency and increased amplitude,  
465 leading to increased entropy.<sup>62</sup> The entropy increase is higher in  
466 the bulk, because more adjacent atoms are relaxed, and the  
467 relaxation from its dense-packed crystal is more dramatic. Thus,  
468 both  $\Delta h_T^0$  and  $\Delta s_T^0$  are negative. Based on the measurements by  
469 Chueh et al.,<sup>44</sup> we obtain  $\Delta h_T^0 = -113.7 \text{ kJ mol}^{-1}$ , and  $\Delta s_T^0 =$   
470  $-50.2 \text{ J mol}^{-1} \text{ K}^{-1}$  for the Sm-doped ceria (see Appendix B for  
471 calculation). 472

**Numerical Simulation.** With the assumption of a uniform  
473 bulk defect concentration, and eq 37 to connect bulk to surface,  
474 we can simplify eq 18 by considering the conservation of the  
475 overall oxygen vacancy within the particle: 476

$$\frac{\partial}{\partial t} (\tilde{\rho}_{Ce} V_R [V_{O}^{\bullet\bullet}]_b) = -S_R \tilde{\rho}_{Ce,s} r_1 \quad (43) \quad 477$$

where  $V_R$  and  $S_R$  are the volume and the surface area of the  
478 particle, and  $\tilde{\rho}_{Ce}$  is the molar density of the unit cell in the bulk.  
479 Equation 43 describes the fact that the surface splitting reaction  
480 leads to the consumption of oxygen vacancy. We note here that  
481 the moles of the oxygen vacancy on the surface is negligible  
482 compared to the bulk, and thus it is neglected from the left-  
483 hand side of eq 43. 484

Equations 17, 37, and 43 form the complete description of  
485 the redox process. The unknown (not all kinetic) parameters  
486 are  $k_{i,\tilde{\rho}}$ ,  $K_i$  ( $i = 1, 2$ ),  $\Delta h_T^0$  and  $\Delta s_T^0$ . With the time-resolved  
487 profiles of  $[H_2O]$  and  $[H_2]$  measured using the QMS, the  
488 entire conversion process can be predicted. These equations are  
489 integrated numerically, and the predicted reactivity is compared  
490 to the experimental measurement. The unknown parameters  
491 are then varied to minimize the difference: 492

$$f = \sum_{\text{all tests}} \sqrt{\sum_{0 \leq t \leq t^*} (\hat{\omega}_{\text{predicted}} - \hat{\omega}_{\text{measured}})^2} \quad (44) \quad 493$$

Here the reaction rates ( $\hat{\omega}_{\text{predicted}}$  or  $\hat{\omega}_{\text{measured}}$ ) are normalized by  
494 the maximum rate in each test. The minimization is performed  
495 numerically in MATLAB using fminsearch solver.<sup>64</sup> The redox  
496 measurements at 600, 700, 800, 900, and 1000 °C are used to  
497 extract the unknown parameters.  $\Delta h_T^0$  and  $\Delta s_T^0$  for Sm-doped  
498 ceria calculated in Appendix B are taken as the initial guess, but 499



500 variations are allowed to account for the difference between  
501 Sm-doped and undoped ceria. To ensure a global minimum,  
502 the initial guess is randomly sampled over a wide range of  
503 values ( $\ln k_0$  from  $-20$  to  $20$ ,  $E$  from  $0$  to  $200$ ) for  $200$  tests,  
504 and the results with minimum  $f$  are chosen.

#### 4. RESULTS

##### 505 **CeO<sub>2</sub> Morphology Evolution and Cyclic Repeatability.**

506 Figure 4 shows the SEM images of the fresh (panel a) and aged

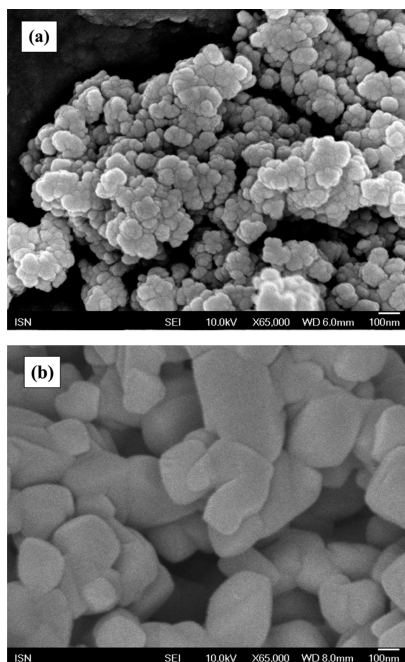


Figure 4. SEM images of ceria powder (a) before redox cycles and (b) after 100 redox cycles.

507 (panel b) ceria powder. It is found that the fresh sample  
508 contains particles of size  $\sim 50$  nm, clumping together into  
509 a mushroom-like structure. During pretreatment, the surface  
510 area is reduced and the particles sinter into an interconnected

structure with a size  $\sim 200$  nm (based on the BET measure-  
511 ment). This structural relaxation is caused by sintering during  
512 the initial redox treatment (first 100 cycles). Samples after  
513 additional 20 redox cycles are also examined, and the same  
514 microstructure and redox rates are obtained, indicating that a  
515 periodic and reversible stationary equilibrium is reached.

516 Figure 5 shows the profiles of H<sub>2</sub> and H<sub>2</sub>O for three redox  
517 cycles at 1000 °C. Reduction proceeds for 2 min with 14% H<sub>2</sub>  
518 at 350 cm<sup>3</sup>(STP)/min, while oxidation with 26% H<sub>2</sub>O for  
519 2 min. Two min Ar purging is used in between to remove  
520 residuals. H<sub>2</sub> spikes with the rise of H<sub>2</sub>O, with the peak H<sub>2</sub>  
521 7%, roughly a quarter of the feed H<sub>2</sub>O. After the peak, H<sub>2</sub> drops  
522 quickly, and diminishes after 0.5 min. The H<sub>2</sub> near the end of  
523 the oxidation phase is essentially zero. After oxidation, the ceria  
524 sample is also tested with 1% O<sub>2</sub> (Ar balance), and no further  
525 consumption of O<sub>2</sub> is observed. This indicates a complete  
526 reoxidation of ceria with H<sub>2</sub>O. Similarly, the produced H<sub>2</sub>O  
527 during reduction spikes at the beginning of each reduction  
528 cycle. The peak H<sub>2</sub>O reaches around 3%, approximately one-  
529 fifth of the feed H<sub>2</sub> during reduction. H<sub>2</sub>O decays slower as  
530 compared to H<sub>2</sub> during oxidation, and approaches zero after  
531 2 min, indicating a slower reactivity compared to oxidation.  
532 The cycles are repeatable with no noticeable difference.  
533 Figure 6 compares the total cumulative H<sub>2</sub> and H<sub>2</sub>O production  
534 during the oxidation and reduction steps, respectively, for eight  
535 cycles measured at 1000 °C. The total H<sub>2</sub> production closely  
536 matches with the H<sub>2</sub>O production, indicating cyclic regener-  
537 ability. The total produced H<sub>2</sub> is about 1250  $\mu\text{mol g}^{-1}$  ceria,  
538 corresponding to a  $\Delta\delta$  of 0.215.

539 **Effect of Temperature.** Figure 7 compares  $\omega_{\text{H}_2}$  and  $\omega_{\text{H}_2\text{O}}$   
540 as a function of temperature from 500 to 1000 °C. In each plot,  
541 the reaction rate exhibits a fast initial stage, followed by a  
542 quick decrease. During oxidation, the fast initial rise of H<sub>2</sub>  
543 corresponds to the rapid ion-incorporation process with the  
544 enriched surface oxygen vacancies, as shown in section 5. The  
545 reactant concentration on the surface plays a significant role  
546 in determining the maximum rate. For temperatures lower than  
547 700 °C, H<sub>2</sub> production is limited, owing to the slow oxygen  
548 removal kinetics and hence limited oxygen vacancy created  
549 in the previous reduction step. Increasing the temperature until  
550

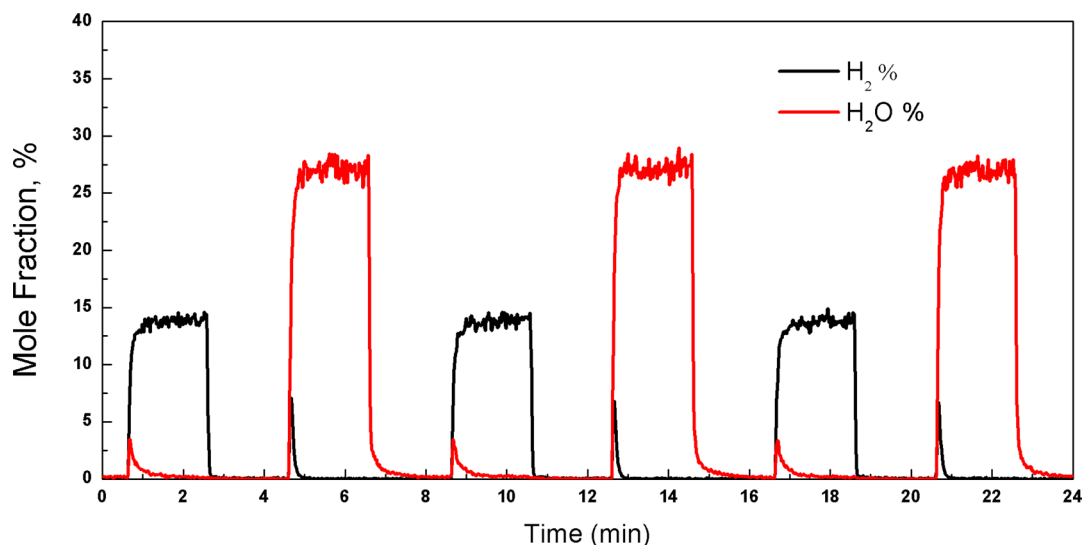


Figure 5. Three redox cycles at 1000 °C with 26% H<sub>2</sub>O for oxidation and 13.7% H<sub>2</sub> for reduction. The redox step takes 2 min each, and the purging section takes 2 min in between. The total CeO<sub>2</sub> is 100 mg.

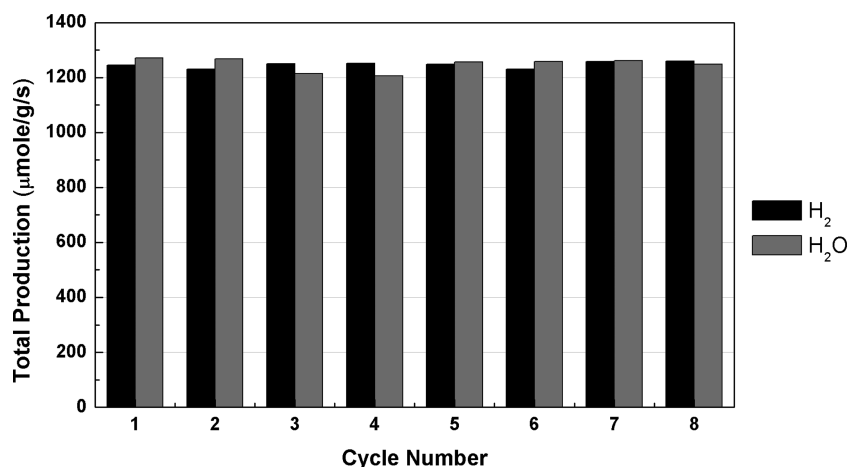


Figure 6. Total H<sub>2</sub> and H<sub>2</sub>O production during the oxidation and reduction, respectively, for eight cycles at 1000 °C.

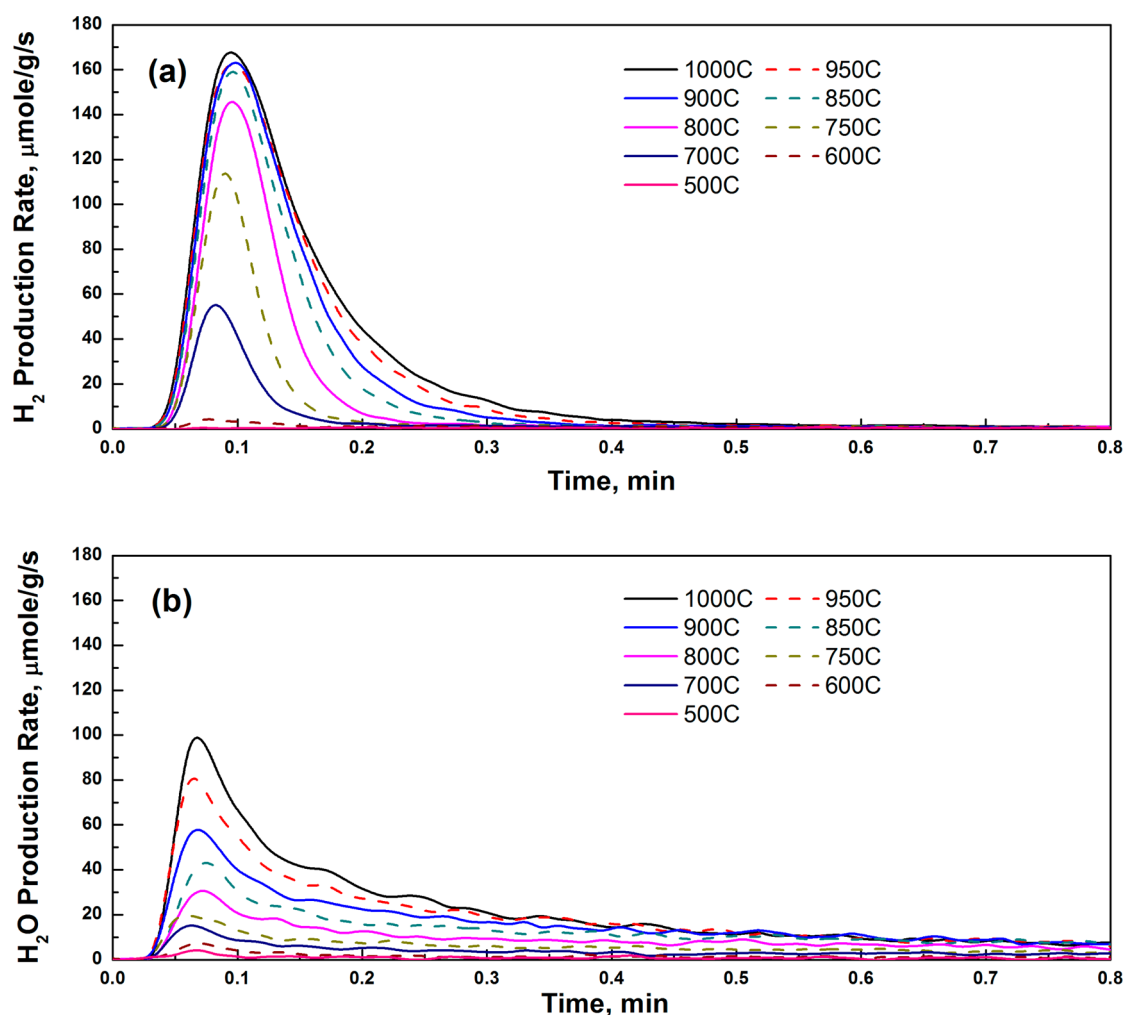


Figure 7. (a) H<sub>2</sub> production rate ( $\mu\text{mol g}^{-1} \text{s}^{-1}$ ) during the oxidation step and (b) H<sub>2</sub>O production rate ( $\mu\text{mol g}^{-1} \text{s}^{-1}$ ) during the reduction step. Temperature is varied from 1000 to 500 °C. 26% H<sub>2</sub>O at 337 cm<sup>3</sup>(STP)/min is used for oxidation, and 14.3% H<sub>2</sub> at 350 cm<sup>3</sup>(STP)/min is used for reduction. The uncertainties of the rate measurements are  $\pm 0.5 \mu\text{mol g}^{-1} \text{s}^{-1}$  for H<sub>2</sub> production, and  $\pm 0.75 \mu\text{mol g}^{-1} \text{s}^{-1}$  for H<sub>2</sub>O production.

551 850 °C leads to a significant jump, and the peak rate doubles  
 552 almost every 50 °C. Further increase in the temperature,  
 553 however, only mildly improves H<sub>2</sub> production rates during the  
 554 initial stage. As will be discussed in section 5, the nonlinear  
 555 temperature dependence is caused by the surface defect  
 556 segregation. Following the peak, H<sub>2</sub> production sharply decays

and approaches zero after 0.5 min, exhibiting linear dependence  
 557 on temperature, as it is mainly controlled by the available  
 558 oxygen vacancy in the bulk phase. 559

560 Compared with oxidation, the reduction step is slower  
 561 and more sensitive to temperature. A fast initial spike is again  
 562 observed, followed by a slower decay. The peak occurs around

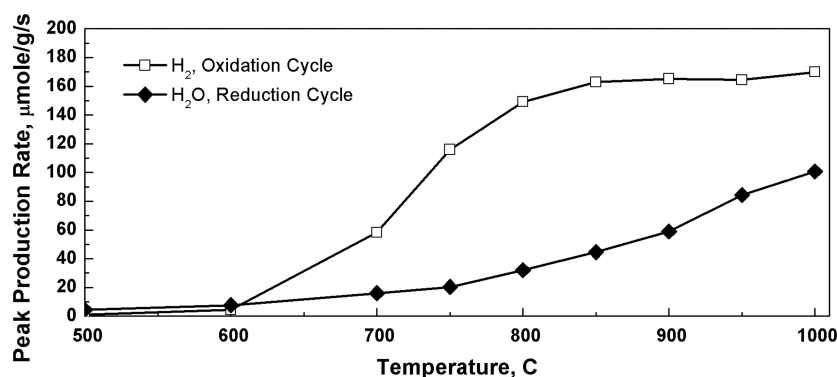


Figure 8. Peak H<sub>2</sub> and H<sub>2</sub>O production rates as a function of temperature during oxidation and reduction cycles.

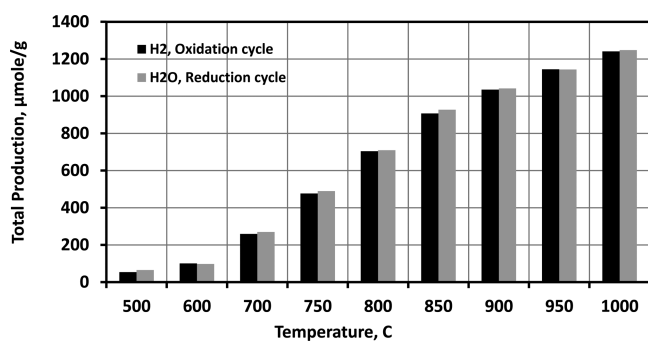


Figure 9. Total H<sub>2</sub> and H<sub>2</sub>O production as a function of temperature during oxidation and reduction steps.

stage, the rise of  $\omega_{\text{H}_2\text{O}}$  depends almost linearly on the temperature throughout the entire range, indicating a large activation energy barrier. However,  $\omega_{\text{H}_2\text{O}}$  profiles start to overlap during the decay stage for temperature above 850 °C, as the removal of oxygen essentially brings the surface closer to the beginning of the oxidation phase, where the segregation effect reduces the difference among different temperatures.

Figure 8 emphasizes the observed behavior of the peak rates at varying temperature. The peak H<sub>2</sub> rate exhibits a sigmoidal profile with a rapid increase around a threshold temperature of 700 °C, while the peak H<sub>2</sub>O rate continuously increases with temperature. The total H<sub>2</sub>/H<sub>2</sub>O production during the 2 min oxidation/reduction process is illustrated in Figure 9. In all the cases, a close match is found between the H<sub>2</sub> and H<sub>2</sub>O production. Governed by the temperature sensitive reduction step, the overall H<sub>2</sub> production rises continuously with temperature. Figure 10 compares

0.08 min similar to that shown in Figure 7a, while the decay continues even after 1 min (see Figure 5). During the initial

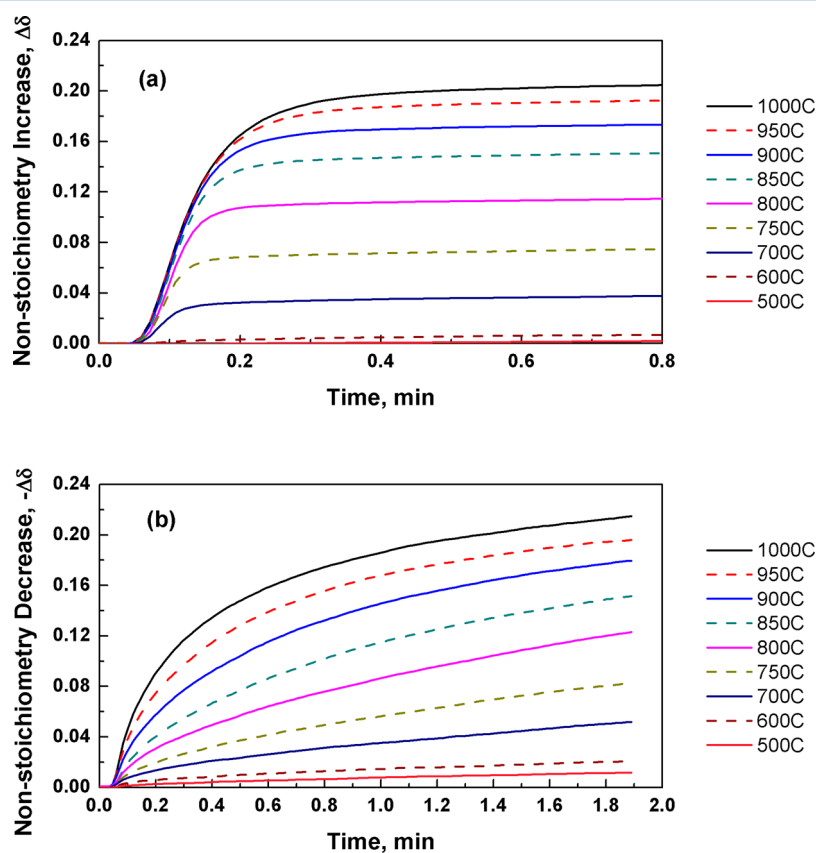
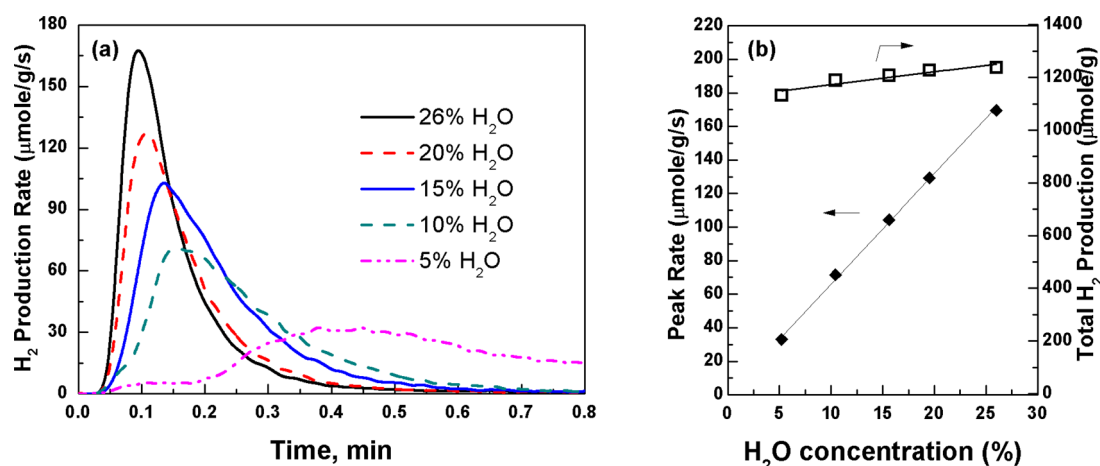
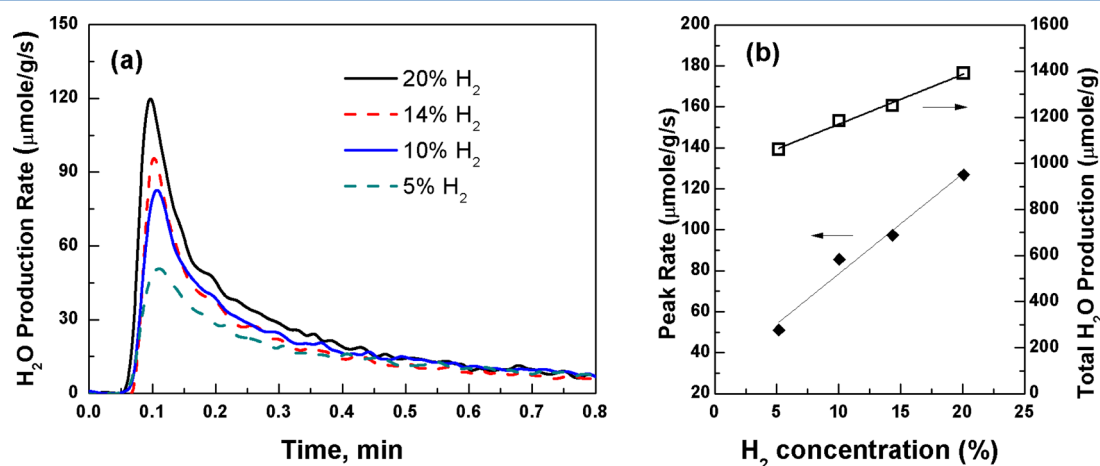


Figure 10. Nonstoichiometry change  $\Delta\delta$  during (a) the oxidation step and (b) the reduction step as a function of temperature.



**Figure 11.** (a) Oxidation rate at different H<sub>2</sub>O concentrations. (b) Peak rate and total production as a function of H<sub>2</sub>O concentration. The temperature is fixed at 1000 °C. The H<sub>2</sub> concentration is fixed at 13.7% during reduction.



**Figure 12.** (a) Reduction rate at different H<sub>2</sub> concentrations. (b) Peak rate and total production as a function of H<sub>2</sub> concentration. The temperature is fixed at 1000 °C. The H<sub>2</sub>O concentration is fixed at 26% during reduction.

**Table 4. Fitted Kinetic Parameters for Both the Forward and Backward Reactions**

	$k$ (s <sup>-1</sup> )	
	reaction 1	reaction 2
forward	$1.3 \times 10^2 \exp((-7.0 \pm 7 \text{ kJ mol}^{-1})/RT)$	$1.5 \times 10^{14} \exp((-190 \pm 50 \text{ kJ mol}^{-1})/RT)$
backward	$8.2 \times 10^{14} \exp((-210 \pm 50 \text{ kJ mol}^{-1})/RT)$	$4.4 \times 10^4 \exp((-97 \pm 5 \text{ kJ mol}^{-1})/RT)$
equilibrium	$1.6 \times 10^{-13} \exp((203 \pm 50 \text{ kJ mol}^{-1})/RT)$	$3.4 \times 10^9 \exp((-93 \pm 50 \text{ kJ mol}^{-1})/RT)$

**Table 5. Parameters for the Transport and Bulk Defect Equilibria**

	CeO <sub>2</sub>			Sm <sub>0.2</sub> Ce <sub>0.8</sub> O <sub>1.9</sub>
	this work	ref 48 <sup>a</sup>	ref 49	ref 44 <sup>b</sup>
$\Delta h_T^0$ (kJ mol <sup>-1</sup> )	-107.6 ± 16.8			-95.7
$\Delta s_T^0$ (J mol <sup>-1</sup> K <sup>-1</sup> )	-54.0 ± 11.9			-26.5
$\Delta h_b^0$ (kJ mol <sup>-1</sup> )	467.4 ± 8.9	455.2	450.2	373.2
$\Delta s_b^0$ (J mol <sup>-1</sup> K <sup>-1</sup> )	172.9 ± 6.4	144.3	131.8	101.5

<sup>a</sup>Note that ref 48 reports varying enthalpy and entropy with  $\delta$ ; the values are averaged for  $\delta = 0-0.05$ . <sup>b</sup>The values are calculated based on the chemical potential of atom oxygen as reported in ref 44. See Appendix B for calculations.

581 the difference in the profiles of the nonstoichiometry  $\Delta\delta$ ,  
582 as calculated in eq 7, during oxidation and reduction. The initial  
583 stage of oxidation ends within 15 s, but accounts for more than  
584 80% of the overall change, and the residual oxidation only leads to  
585 a minor increase. Raising the temperature enlarges the overall  
586 oxygen carrying capacity, but the conversion follows a similar

pattern. In comparison, reduction proceeds more gradually, and it  
587 is more temperature sensitive. The transition between the initial  
588 and residual stages is less obvious, and both stages equally  
589 contribute to the overall nonstoichiometry change. The reduction  
590 continues after 2 min although the rate is too slow to be of  
591 practical interest. 592

593 The measured peak  $H_2$  rate is  $\sim 160 \mu\text{mol g}^{-1}\text{s}^{-1}$  at  $1000^\circ\text{C}$   
 594 and  $60 \mu\text{mol g}^{-1}\text{s}^{-1}$  at  $700^\circ\text{C}$  (also included in Table 2 for  
 595 comparison). The fast  $H_2$  production rate is because of the fine  
 596 particles, and hence large surface area, used in the measurements.  
 597 Comparing to TCWS, the utilization of fuel in the reduction step  
 598 creates many oxygen vacancies and hence leads to an enhanced  
 599  $H_2$  production. The oxygen removal in reduction is the limiting  
 600 step and is more temperature sensitive.  $700^\circ\text{C}$  is the threshold  
 601 temperature to achieve a large oxygen nonstoichiometry and  
 602 hence enables a transition to a fast  $H_2$  production rate in the  
 603 following oxidation step. Therefore,  $700^\circ\text{C}$  (or above) along  
 604 with a longer residence time in reduction is beneficial.

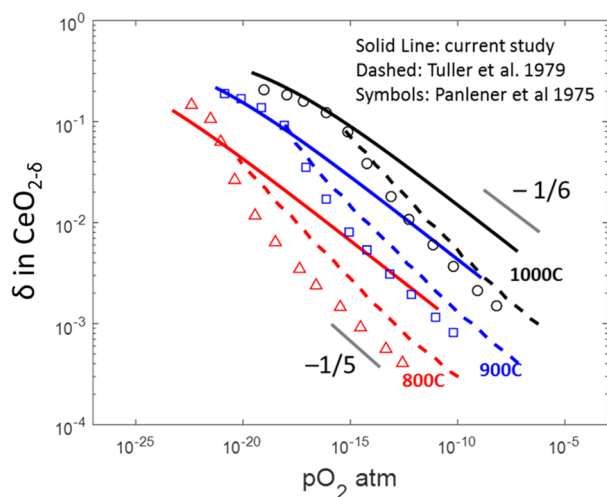


Figure 13. Isothermal oxygen nonstoichiometry as a function of  $p_{O_2}$  for  $CeO_{2-x}$  from 800 to  $1000^\circ\text{C}$  (solid lines). Dashed lines are based on the conductivity measurements by Tuller and Nowick.<sup>49</sup> Symbols are from Panlener et al.<sup>48</sup> Gray lines are for guiding the eyes.

Effect of  $H_2O/H_2$  Concentration. Figure 11 and Figure 12 show the effect of  $H_2O$  and  $H_2$  concentration, respectively. The measured rates are plotted in panel a, while the peak rate and the total production are highlighted in panel b.  $\omega_{H_2}$  becomes taller and narrower at higher  $H_2O$  concentration. The peak rate linearly depends on the  $H_2O$  concentration, while the total production remains the same. In contrast, a stronger reducing environment shifts the entire  $\omega_{H_2O}$  curve outwardly and hence enlarges the overall oxygen carrying capacity. The peak rate also linearly depends on the  $H_2$  concentration.

## 5. DISCUSSION

The kinetics and the defect equilibrium parameters derived in this study for undoped ceria are summarized in Table 4 and Table 5. The values of  $\Delta h_b^0$  and  $\Delta s_b^0$  are close to those obtained for Sm-doped ceria (see Appendix B). The bulk equilibrium for reaction 40 is also calculated by combining eqs 9, 10, and 39 along with the water splitting reaction,  $H_2(g) + \frac{1}{2}O_2(g) = H_2O(g)$ , as

$$K_b = \exp\left(-\frac{\Delta h_b^0 - T\Delta s_b^0}{RT}\right) = \frac{p_{O_2}^{1/2} [V_{O^{\bullet\bullet}}]_b [Ce'_{Ce}]_b^2}{[O_O^{\times}]_b [Ce^{\times}_{Ce}]_b^2} = (K_1 K_2 K_T K_W)^{-1} \quad (45)$$

Here  $K_1$ ,  $K_2$ ,  $K_T$ , and  $K_W$  are the equilibrium constants for the surface reactions R1 and R2, the bulk-to-surface transport, and the water splitting reaction, respectively. The calculated bulk-phase equilibrium ( $\Delta h_b^0$  and  $\Delta s_b^0$ ) is in a close match with the literature,<sup>48,49</sup> as shown in Table 5. Figure 13 depicts the isothermal bulk oxygen vacancy concentration as a function of the equivalent  $p_{O_2}$ , compared with the measurements reported by Panlener et al.<sup>48</sup> and Tuller and Nowick.<sup>49</sup> Quantitative agreement is found at large nonstoichiometry, although discrepancy

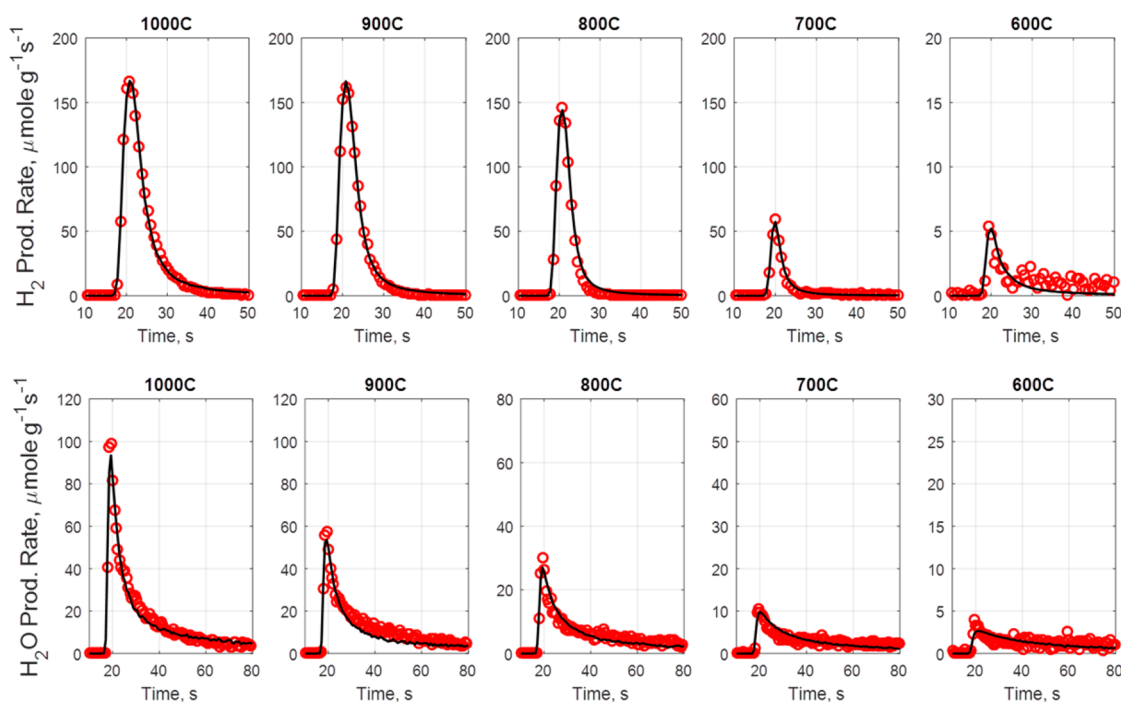


Figure 14. Comparison between the model predictions (lines) and the measurements (circles) for both oxidation (upper panels) and reduction (lower panels). The scales in the y-axis are different at lower temperature for clarity.

632 is seen when  $p_{\text{O}_2}$  is high, resulting from a slightly larger  $\Delta h_{\text{b}}^0$ .  
 633 Both ref 49 and the current study report a dependence of  $-1/6$   
 634 near stoichiometry, while Panlener et al.<sup>48</sup> reported a depen-  
 635 dence close to  $-1/5$ , possibly due to the existence of impurities.<sup>47</sup>  
 636 Figure 14 shows a comparison between the measured reactiv-  
 637 ity and model predictions for both oxidation and reduction.

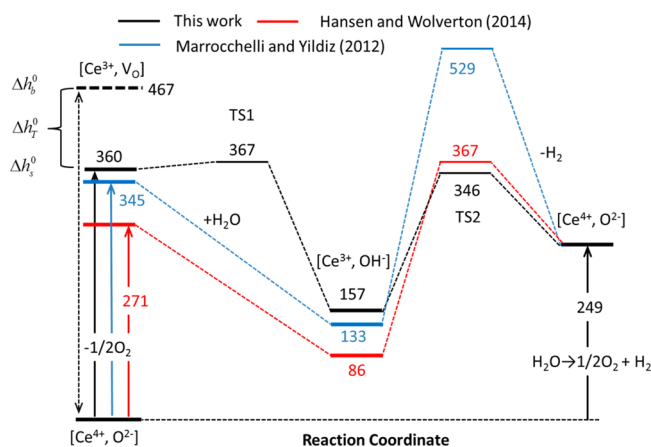


Figure 15. Energy landscape for the reaction pathway (black), and comparison with the theoretical calculations by Hansen and Wolverton<sup>52</sup> (red) and Marrocchelli and Yildiz<sup>51</sup> (blue). The dashed black line on the left side denotes the bulk-phase defect.  $\Delta h_{\text{b}}^0$  and  $\Delta h_{\text{s}}^0$  denote the defect formation energy for bulk (eq 40) and surface (eq 41), respectively, and  $\Delta h_{\text{t}}^0$  denotes the difference. Unit is  $\text{kJ mol}^{-1}$ .

An excellent match is found for all cases. The predictions well-characterize the spike–decay behaviors of both redox steps. The temperature dependence is precisely represented; the subtle difference between the reduction and oxidation steps is also adequately captured.

Figure 15 shows the calculated energy landscape (black lines) for the surface chemistry (see Table 4). The energy levels for the intermediate species on the surface as well as the transition states are plotted in reference to the perfect crystal as the ground state. R1 is highly exothermic with a minor barrier. The second step is highly endothermic, and requires a significant energy to break up the O–H bond. The intermediate species,  $\text{OH}_{\text{O}}^*$ , lies in a deep valley, and hence one may expect high surface coverage at low temperature. The overall  $\text{H}_2$  production process (eq 8) is exothermic with the enthalpy of reaction around  $-120 \text{ kJ mol}^{-1}$ . The theoretical calculations by Hansen and Wolverton<sup>52</sup> (red lines) and Marrocchelli and Yildiz<sup>51</sup> (blue lines) are also included in this plot for comparison. Both obtained similar reaction energy for the first step, although they split it and simulated the adsorption and the dissociation processes separately. Similarly, no substantial activation barriers were found for R1 in either work. Marrocchelli and Yildiz<sup>51</sup> modeled the breaking of the O–H bond as a symmetric process and reported a significant barrier around  $400 \text{ kJ mol}^{-1}$  for  $\text{H}_2$  formation. In contrast, Hansen and Wolverton<sup>52</sup> identified an asymmetric pathway with a much lower barrier ( $281 \text{ kJ mol}^{-1}$ ). The current study reported a barrier around  $200 \text{ kJ mol}^{-1}$ . The lower barrier may result from alternative fast desorption

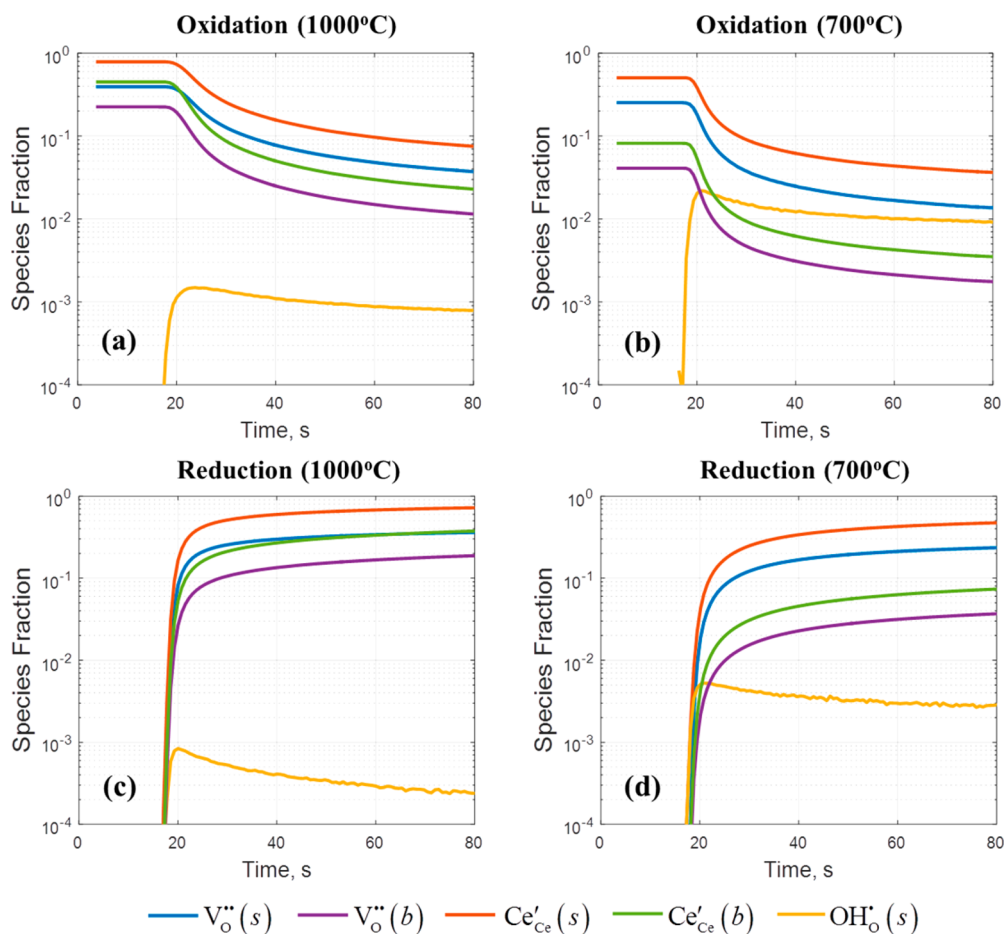


Figure 16. Concentrations of the bulk and surface species for oxidation (a, b) and reduction (c, d) at 1000 and 700 °C.

666 pathways, especially at large nonstoichiometry when the surface  
 667 defect vacancy concentrations are high. Marrocchelli and  
 668 Yildiz<sup>51</sup> reported a similar overall energy of reaction ( $\Delta h_s^0$  for  
 669 eq 41) as in this study, while Hansen and Wolverson<sup>52</sup> reported  
 670 a slightly lower value. The bulk-phase defect formation energy,  
 671  $\Delta h_b^0$ , is also included in Figure 15, and the difference between  
 672 the bulk and the surface is  $\Delta h_T^0$ .

673 Figure 16 plots the species concentration in the bulk and on the  
 674 surface. The reduction reaction starts from stoichiometry  
 675 (complete oxidation from the previous step), while oxidation  
 676 begins with the defects determined from the previous reduction  
 677 step. During the oxidation step, all species undergo a quick  
 678 decay, leading to a rapid  $H_2$  production during the initial stage  
 679 as observed in Figure 7. The initial stage is followed by a much  
 680 slower decay as the conversion transits to the second stage  
 681 where the species concentrations are mainly affected by the  
 682 equilibrium with the  $H_2O/H_2$  environment. Hydroxyl is quickly  
 683 formed as the reaction starts and remains in a quasi-steady state  
 684 during the rest of the process. Low temperature favors the  
 685 formation of hydroxyl ions, owing to the large energy barriers  
 686 as seen in Figure 15. The bulk defect concentrations are highly  
 687 sensitive to temperature, as evident from the large  $\Delta h_b^0$  shown  
 688 in Table 5, leading to a significant difference between the high  
 689 and the low temperature cases. On the other hand, the surface  
 690 defect is less dependent on the temperature. In all cases, the  
 691 concentrations on the surface are observed to be much higher  
 692 than the bulk. The surface segregation effect is more significant  
 693 at low temperature, causing over an order-of-magnitude  
 694 improvement compared to the bulk phase. Similar behavior is  
 695 observed during the reduction step, where the segregation  
 696 effect is more pronounced near the end of conversion.

697 To further examine the surface segregation effect, Figure 17a  
 698 shows the calculated equilibrium concentration of  $Ce'_{Ce}$  in the  
 699 bulk and on the surface as a function of the effective  $p_{O_2}$ . Each  
 700 line corresponds to the same range of  $H_2O:H_2$  ratio, from  $10^{-3}$   
 701 (reducing) to  $10^3$  (oxidizing). Under all conditions, the surface  
 702  $[Ce'_{Ce}]$  value is significantly greater than the bulk, indicating  
 703 that the surface is more reduced. The ratio between surface and  
 704 bulk, as shown in Figure 17b, ranges from 1.5 to 15, favoring  
 705 the low temperature. Apart from the difference in the absolute  
 706 values, the temperature and oxygen dependence also differs  
 707 remarkably between bulk and surface.  $[Ce'_{Ce}]$  on the surface is  
 708 only weakly sensitive to temperature and becomes almost the  
 709 same above 800 °C (with  $H_2O:H_2$ ), causing the overlap of the  
 710 measured reaction rates during the first stage of oxidation  
 711 (Figure 7a) and the second stage of reduction (Figure 7b).  
 712  $[Ce'_{Ce}]$  in the bulk generally exhibits  $-1/6$  dependence on the  
 713  $p_{O_2}$ , as expected from eq 45. On the other hand, the  $p_{O_2}$   
 714 dependence for surface  $[Ce'_{Ce}]$  flattens from  $-1/6$  with decreasing  
 715  $p_{O_2}$  and eventually goes to zero as the surface becomes fully  
 716 reduced. This nonlinearity results from the reduced concentration  
 717 of the normal sites ( $O_{O}^{\times}$ ,  $Ce'_{Ce}$  in eq 45) on the surface.  
 718 As a result, the ratio in panel b exhibits a nonlinear pattern  
 719 with  $p_{O_2}$ .

720 Figure 18 shows the forward and the backward reaction rates  
 721 for the redox processes. At all temperatures, the  $H_2O$  adsorp-  
 722 tion and dissociation step (R1) during oxidation is much faster;  
 723 equilibrium is quickly established and maintained throughout  
 724 the rest of the conversion. In contrast, the ion/electron-transfer  
 725 process (R2) is slower and its backward reaction rate is close  
 726 to zero. This indicates that the reaction is limited by the  
 727 charge-transfer process (R2), as also observed by Feng et al.<sup>45</sup>

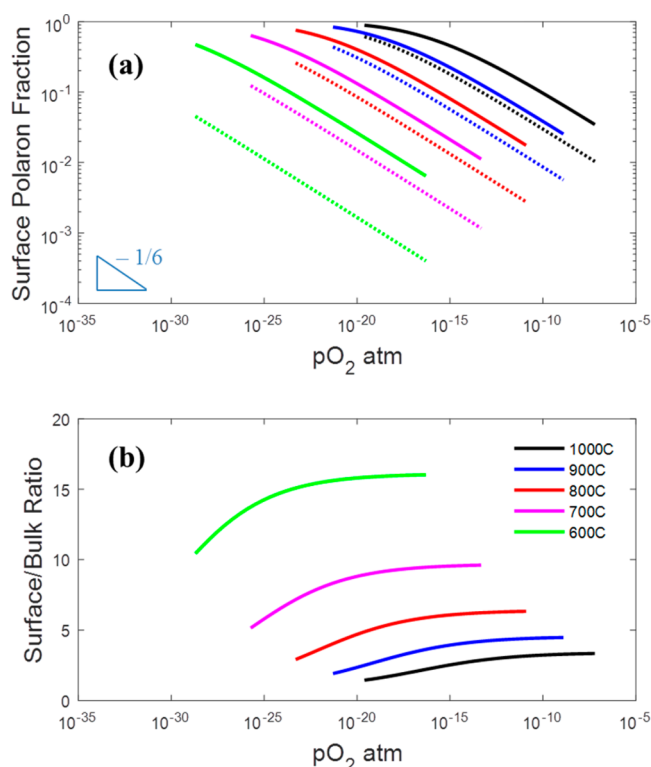


Figure 17. (a)  $Ce'_{Ce}$  concentration at equilibrium on the surface (solid) and in the bulk (dashed). Value of 1 corresponds to a complete reduction to the reduced 3+ state. (b) Ratio of the surface to bulk  $Ce'_{Ce}$  concentration.

728 Compared to oxidation, the reduction rate is much slower. 728  
 729 The forward and backward rates for both steps are at similar 729  
 730 magnitude, and equilibria are established during most of the 730  
 731 conversion process. The low rates for R1 are mainly attributed 731  
 732 to the low  $H_2O$  produced during reduction. A more reducing 732  
 733 environment (e.g., higher  $H_2$  concentration) effectively shifts 733  
 734 the equilibrium backward, leading to more reduced ceria, as 734  
 735 observed in Figure 12. 735

736 The surface segregation effect along with the plausible rate- 736  
 737 limiting step observed in this study suggests directions for 737  
 738 improving the water splitting activity of ceria and potentially 738  
 739 other oxygen-incorporation materials. The reduction step is in 739  
 740 general much slower, and it limits the redox capability at low 740  
 741 temperature ( $\leq 700$  °C). Therefore, promoting the reduction 741  
 742 step is essential to the low temperature water splitting process. 742  
 743 On the other hand, the surface is nearly enriched with the 743  
 744 defects at high temperature ( $>700$  °C), and the overall  $H_2$  744  
 745 production is constrained by the charge-transfer step. Thus, 745  
 746 efforts should concentrate on accelerating the charge-transfer 746  
 747 step at high temperature. 747

## 6. CONCLUSIONS

748 This work presents a detailed redox study with emphasis on 748  
 749 identifying the surface ion-incorporation kinetics pathway. 749  
 750 Time-resolved kinetics is measured for ceria nanopowder in a 750  
 751 button cell reactor for 600–1000 °C at atmospheric pressure. 751  
 752 The ceria sample is alternatively exposed to water vapor in 752  
 753 the oxidation cycle to produce  $H_2$  and  $H_2/Ar$  mixture in the 753  
 754 reduction cycle to remove the lattice oxygen. The ceria sample 754  
 755 undergoes structural and morphological changes during the 755  
 756 initial redox treatment before reaching cyclic equilibrium. 756

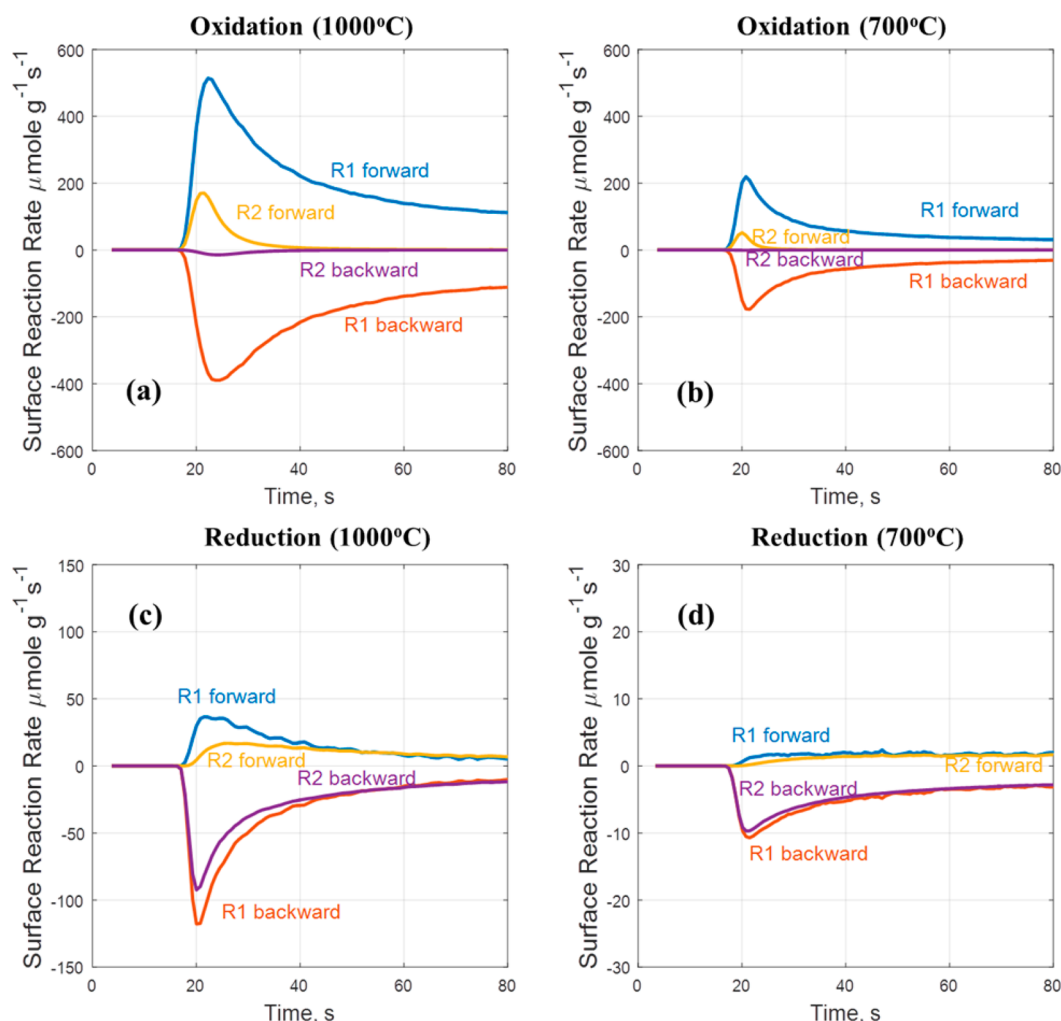


**Figure 18.** Surface reaction rates for both steps in oxidation (a, b) and reduction (c, d). The forward reaction rates are plotted as positive values, and the backward rates are negative. Note different scales are used in panels c and d for clarity.

757 We find an over 1 order-of-magnitude higher H<sub>2</sub> production  
 758 rate compared to the state-of-art thermochemical water  
 759 splitting and reactive chemical-looping water splitting studies.  
 760 The high redox rates are attributed to the fine particles  
 761 and hence large surface areas used in the study, which ensure  
 762 a surface-limited-process. The peak rates measured are  
 763 160 μmol g<sup>-1</sup>s<sup>-1</sup> at 1000 °C and 60 μmol g<sup>-1</sup>s<sup>-1</sup> at 700 °C.  
 764 The maximum nonstoichiometry change (Δδ) achieved is  
 765 0.215 at 1000 °C. It is found that the H<sub>2</sub> production rate  
 766 depends weakly on temperature in the range 800–1000 °C,  
 767 while the reduction process critically depends on the reaction  
 768 temperature. Overall, reduction is the limiting step especially  
 769 at low temperature, and it determines the total amount of the  
 770 hydrogen produced in the following oxidation step.

771 The redox kinetics is modeled using a two-step surface  
 772 chemistry while considering bulk-to-surface transport equilibrium.  
 773 The proposed surface chemistry comprises an H<sub>2</sub>O adsorption/  
 774 dissociation step and a charge-transfer step. Kinetics and equi-  
 775 librium parameters are extracted and excellent agreement is  
 776 achieved between the model predictions and the measurements.  
 777 Driven by the difference in the free energy of formation, the  
 778 surface defect concentration is found to be an order-of-magnitude  
 779 higher than the bulk. The model reveals that the surface defects  
 780 are abundant during the redox conditions, and the charge-  
 781 transfer process is the rate-determining step for H<sub>2</sub> production.

The kinetic model along with the surface-controlled experiments  
 provides a new approach to examine the redox pathways and  
 defect equilibrium for alternative materials. The kinetics study  
 also provides guidance for the design and the practical applica-  
 tion of the chemical-looping water splitting technology: (1) finer  
 particles are preferred to enable faster kinetics; (2) the operating  
 temperature is recommended to be higher than the threshold  
 700 °C to ensure fast redox conversion; (3) an oxidation period  
 less than 30 s suffices to regenerate the oxygen vacancy while a  
 slightly longer residence time in reduction is beneficial.

## APPENDIX A

The diffusion flux for V<sub>O</sub><sup>••</sup> and Ce'<sub>Ce</sub> can be expressed as

$$-\frac{J_{V_O^{\bullet\bullet}}}{\tilde{\rho}_{Ce}[V_O^{\bullet\bullet}]D_{V_O^{\bullet\bullet}}} = \frac{\partial[V_O^{\bullet\bullet}]}{\partial r} \left( \frac{1}{[V_O^{\bullet\bullet}]} + \frac{l}{2 - [V_O^{\bullet\bullet}]} \right) + \frac{2F}{RT} \frac{\partial\phi}{\partial r} \quad (\text{A1})$$

$$-\frac{J_{Ce'_{Ce}}}{\tilde{\rho}_{Ce}[Ce'_{Ce}]D_{Ce'_{Ce}}} = \frac{\partial[Ce'_{Ce}]}{\partial r} \left( \frac{1}{[Ce'_{Ce}]} + \frac{l}{1 - [Ce'_{Ce}]} \right) - \frac{F}{RT} \frac{\partial\phi}{\partial r} \quad (\text{A2})$$

Here we consider the region sufficiently away from the surface,  
 such that the defect segregation effect is not important (i.e., μ<sub>i</sub><sup>0</sup>  
 is constant).



799 Eliminating the electrostatic potential, we have

$$\begin{aligned} & -\frac{J_{V_{O}^{\bullet\bullet}}}{\tilde{\rho}_{Ce}[V_{O}^{\bullet\bullet}]D_{V_{O}^{\bullet\bullet}}} - \frac{2J_{Ce'_{Ce}}}{\tilde{\rho}_{Ce}[Ce'_{Ce}]D_{Ce'_{Ce}}} \\ & = \frac{\partial[V_{O}^{\bullet\bullet}]}{\partial r} \left( \frac{1}{[V_{O}^{\bullet\bullet}]} + \frac{1}{2 - [V_{O}^{\bullet\bullet}]} \right) \\ & \quad + \frac{2\partial[Ce'_{Ce}]}{\partial r} \left( \frac{1}{[Ce'_{Ce}]} + \frac{1}{1 - [Ce'_{Ce}]} \right) \end{aligned} \quad (A3)$$

801 The electroneutrality assumption in the bulk phase requires that  
802 charge neutral:

$$803 \quad 2[V_{O}^{\bullet\bullet}] = [Ce'_{Ce}] \quad (A4)$$

804 zero net current:

$$805 \quad 2J_{V_{O}^{\bullet\bullet}} = J_{Ce'_{Ce}} \quad (A5)$$

806 With substitution of eqs A4 and A5 into A3, we have

$$807 \quad J_{V_{O}^{\bullet\bullet}} = -\tilde{D} \frac{\partial C_{V_{O}^{\bullet\bullet}}}{\partial r} \quad (A6)$$

808 where

$$\tilde{D} = \frac{3D_{V_{O}^{\bullet\bullet}}D_{Ce'_{Ce}}}{D_{Ce'_{Ce}} + 2D_{V_{O}^{\bullet\bullet}}} \left( 1 + \frac{[V_{O}^{\bullet\bullet}]}{6 - 3[V_{O}^{\bullet\bullet}]} + \frac{4[V_{O}^{\bullet\bullet}]}{3 - 6[V_{O}^{\bullet\bullet}]} \right)$$

809  $\tilde{D}$  is the chemical (or ambipolar) diffusion coefficient, which  
810 critically depends on the operating condition, as well as the  
811 dopant/impurity concentrations. A range of values have been  
812 reported in the literature. To evaluate the contribution of the  
813 solid-phase diffusion to the overall redox process, we use the  
814 chemical diffusivity reported by Stan et al.,<sup>63</sup> which is in the  
815 lower range of the available data in the literature (see ref 57 for  
816 comparison) and, hence, leads to an estimation of the upper  
817 bound for the diffusional resistance.

818 The governing equations for  $V_{O}^{\bullet\bullet}$  in the bulk phase can be  
819 expressed as

$$820 \quad \frac{\partial C_{V_{O}^{\bullet\bullet}}}{\partial t} + \frac{1}{r^2} \frac{\partial}{\partial r} (r^2 J_{V_{O}^{\bullet\bullet}}) = 0 \quad (A7)$$

821 With substitution of eq A6 into eq A7, we have

$$822 \quad \frac{\partial C_{V_{O}^{\bullet\bullet}}}{\partial t} = \frac{1}{r^2} \frac{\partial}{\partial r} \left( r^2 \tilde{D} \frac{\partial C_{V_{O}^{\bullet\bullet}}}{\partial r} \right) \quad (A8)$$

823 with initial condition

$$824 \quad C_{V_{O}^{\bullet\bullet}}(t=0) = C_{V_{O}^{\bullet\bullet},0} \quad (A9)$$

825 and the following boundary conditions:

$$826 \quad s\tilde{D} \frac{\partial C_{V_{O}^{\bullet\bullet}}}{\partial r} \Big|_{r=R} = \omega \quad (A10)$$

$$827 \quad \frac{\partial C_{V_{O}^{\bullet\bullet}}}{\partial r} \Big|_{r=0} = 0 \quad (A11)$$

828 In eq A9,  $s$  is the surface area, as listed in Table 3.  $\omega$  is the  
829 surface  $H_2$  (or  $H_2O$ ) production rate (unit,  $\text{mol s}^{-1}$ ). Equations  
830 A8–A11 are solved for the oxidation reaction of the particle  
831 with  $R = 100$  nm. The peak  $H_2$  production rate at each  
832 temperature is used to represent  $\omega$ , and  $\Delta\delta$  is used as the initial

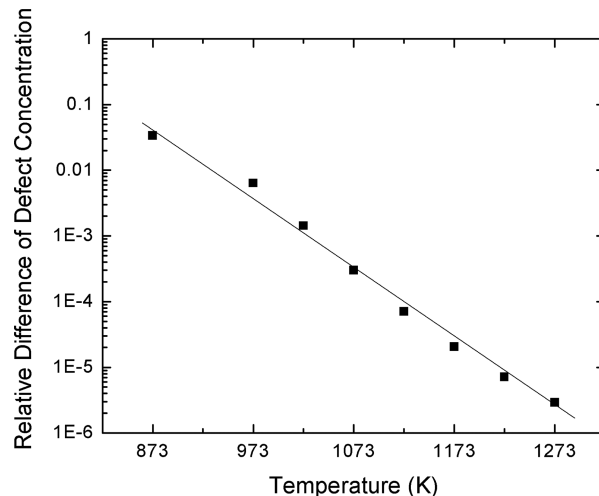


Figure 19. Relative difference of the oxygen vacancy concentration between the center and the surface. Line is for guiding the eyes.

condition. Calculation shows an upper bound for the diffusional  
833 contribution. Figure 19 plots the normalized difference of  $C_{V_{O}^{\bullet\bullet}}$   
834 between the center and the surface:  
835

$$\Delta = \frac{C_{V_{O}^{\bullet\bullet}}(r=0) - C_{V_{O}^{\bullet\bullet}}(r=R)}{C_{V_{O}^{\bullet\bullet}}(r=R)} \quad \text{when } C_{V_{O}^{\bullet\bullet}}(r=R) = \frac{1}{2}C_{V_{O}^{\bullet\bullet},0} \quad (A12) \quad 836$$

From Figure 19, the maximum difference is found to be less  
837 than 4% at 600 °C and reduces to less than 0.001% at 1000 °C.  
838 Calculation here indicates that the bulk diffusion is unlikely to  
839 be rate-limiting in the redox process.  
840

## 841 ■ APPENDIX B

Chueh et al.<sup>44</sup> measured both the bulk and the surface con-  
842 centration  $Ce^{3+}$  (or  $Ce_{Ce}$ ) for  $Sm_{0.2}Ce_{0.8}O_{1.9}$  under equilibrium  
843 for the temperatures at 466, 521, 586, and 650 °C. The authors  
844 compared the chemical potential of atomic oxygen for the  
845 surface and bulk and attributed the higher concentration of  
846 surface  $Ce^{3+}$  to the higher entropy of the surface oxygen. Here,  
847 we take into account the difference of the defect formation  
848 energy as well as the entropy and present a detailed analysis  
849 following an approach similar to that detailed in section 3 (see  
850 Figure 3),  
851

The site conservation and electroneutrality conditions are 852

$$853 \quad [V_{O}^{\bullet\bullet}] + [O_{O}^{\times}] = 1.9 \quad (B1)$$

$$854 \quad [Ce'_{Ce}] + [Ce_{Ce}^{\times}] + [Sm'_{Ce}] = 1 \quad (B2)$$

$$855 \quad 2[V_{O}^{\bullet\bullet}] = [Sm'_{Ce}] + [Ce'_{Ce}] \quad (B3)$$

In the bulk phase,  $[Sm'_{Ce}]_b = 0.2$ . By substituting eqs B1–B3  
856 into eq 45, and fitting with respect to the measurements of the  
857 bulk  $[Ce'_{Ce}]$  and  $p_{O_2}^{1/2}$ , we obtain the equilibrium constant for  
858 the bulk-phase defects,  $K_b$ :  
859

$$860 \quad K_b = \exp \left( -\frac{\left( 379.5 \frac{\text{kJ}}{\text{mol}} \right) - \left( 97.1 \frac{\text{J}}{\text{mol K}} \right) T}{RT} \right) \quad (B4)$$

The bulk-to-surface transport equilibrium is described by  
861 eq 37. The dopant concentration on the surface,  $[Sm'_{Ce}]_s$ , is in  
862 the range between 0.26 and 0.35, slightly greater than the bulk.  
863

864 For simplicity, we use  $[Sm'_{Ce}]_s = 0.3$ . Note here the right-hand  
865 side of eq B1 becomes 1.85 for the surface ( $Sm_{0.3}Ce_{0.7}O_{1.85}$ ).  
866 By substituting eqs B1–B3 into eq 37, and comparing with  
867 the measurements of the surface  $[Ce'_{Ce}]$  at given temperature  
868 and oxygen partial pressure, we obtain the equilibrium constant  
869 for the transport,  $\Delta\mu_T^0$ :

$$\Delta\mu_T^0 = \left(-113.7 \frac{\text{kJ}}{\text{mol}}\right) - \left(-50.2 \frac{\text{J}}{\text{mol K}}\right)T \quad (\text{B5})$$

871 The model predictions are plotted in Figure 20 along with  
872 the measurements, and an excellent agreement is found for  
873 both the surface and the bulk defect concentrations.

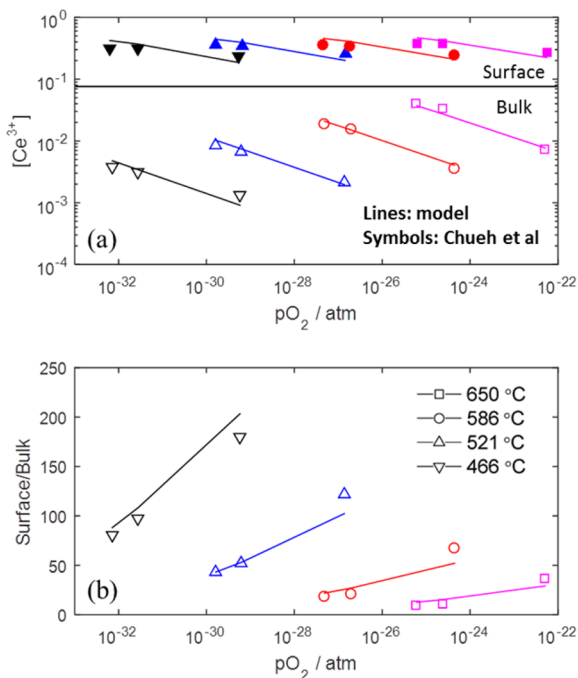


**Figure 20.** (a) Comparison of the surface (closed) and bulk Ce<sup>3+</sup> concentrations between the measurements (symbols) by Chueh et al.<sup>44</sup> and the model predictions (lines). (b) Ratio of the surface to bulk Ce<sup>3+</sup> concentrations. Symbols are from ref 44, and lines are from the modeling.

874 It is interesting to note that compared to the bulk, the surface  
875 has 30% less defect formation enthalpy and over 50% less  
876 defect formation entropy. The ratio of the surface-to-bulk Ce<sup>3+</sup>  
877 is highest at low temperature and drops dramatically as the  
878 temperature is raised. Crossover,  $\Delta\mu_T^0 = 0$ , is reached when  
879  $T = 2265$  K, approaching the melting point.

880 Chueh et al.<sup>44</sup> reported the chemical potential of atomic  
881 oxygen for the surface and bulk, defined as

$$\mu_O = \frac{1}{2}\mu_{O_2} = \frac{1}{2}(\mu_{O_2}^0 + RT \ln p_{O_2}) \quad (\text{B6})$$

883 where  $\mu_{O_2}^0$  is the standard potential at 1 atm.  $\mu_O$  can further  
884 be related to the partial molar enthalpy ( $H_O$ ) and entropy  
885 ( $S_O$ ) from  $\mu_O = H_O - TS_O$ . The reported  $H_O$  and  $S_O$  are  
886  $-373.2$  kJ mol<sup>-1</sup> and  $-86.1$  J mol<sup>-1</sup> K<sup>-1</sup> for  $[Ce^{3+}]_{\text{bulk}} = 0.0071$ ,  
887 and  $-277.5 \pm 28.7$  kJ mol<sup>-1</sup> and  $28.7 \pm 28.7$  J mol<sup>-1</sup> K<sup>-1</sup> for  
888  $[Ce^{3+}]_{\text{surf}} = 0.36$ .

889 To relate the partial molar free energy of the oxygen atom to the  
890 defect formation free energy, we consider the defect formation  
891 reaction, eqs 40 and 41, at equilibrium. The Gibbs free energy is

zero:  $\Delta G = 0 = \mu_{V_{O}^{\bullet\bullet}} + 2\mu_{Ce'_{Ce}} + \frac{1}{2}\mu_{O_2} - \mu_{O_O^{\times}} - 2\mu_{Ce_{Ce}}$ . With  
substitution of eqs 27 and B6, we obtain

$$\begin{aligned} \mu_O &= H_O - TS_O \\ &= -(\mu_{V_{O}^{\bullet\bullet}}^0 + RT \ln[V_{O}^{\bullet\bullet}]) + 2\mu_{Ce'_{Ce}}^0 + 2RT \ln[Ce'_{Ce}] - \mu_{O_O^{\times}}^0 \\ &\quad - RT \ln[O_O^{\times}] - 2\mu_{Ce_{Ce}^{\times}}^0 - 2RT \ln[Ce_{Ce}^{\times}] \\ &= -\left\{ (h_{V_{O}^{\bullet\bullet}}^0 + 2h_{Ce'_{Ce}}^0 - h_{O_O^{\times}}^0 - 2h_{Ce_{Ce}^{\times}}^0) \right. \\ &\quad \left. - T(s_{V_{O}^{\bullet\bullet}}^0 + 2s_{Ce'_{Ce}}^0 - s_{O_O^{\times}}^0 - 2s_{Ce_{Ce}^{\times}}^0) + RT \ln \left[ \frac{[V_{O}^{\bullet\bullet}][Ce'_{Ce}]^2}{[O_O^{\times}][Ce_{Ce}^{\times}]^2} \right] \right\} \end{aligned} \quad (\text{B7})$$

Therefore,

$$H_O = -\left(\Delta h^0 - \frac{1}{2}h_{O_2}^0\right) \quad (\text{B8})$$

$$S_O = -\left(\Delta s^0 - R \ln \left[ \frac{[V_{O}^{\bullet\bullet}][Ce'_{Ce}]^2}{[O_O^{\times}][Ce_{Ce}^{\times}]^2} \right] - 0.5s_{O_2}^0\right) \quad (\text{B9})$$

where  $\Delta h^0$  and  $\Delta s^0$  are the defect formation energy and entropy.  
Based on the reported values for  $H_O$  and  $S_O$ , we obtain  $\Delta h_b^0 =$   
373.2 kJ mol<sup>-1</sup> and  $\Delta s_b^0 = 101.5$  J mol<sup>-1</sup> K<sup>-1</sup> for  $[Ce^{3+}]_{\text{bulk}} =$   
0.0071, and  $\Delta h_s^0 = 277.5 \pm 28.7$  kJ mol<sup>-1</sup> and  $\Delta s_s^0 = 75.0 \pm$   
28.7 J mol<sup>-1</sup> K<sup>-1</sup> for  $[Ce^{3+}]_{\text{surf}} = 0.36$ . Therefore, the differences  
between the surface and the bulk are  $\Delta h_T^0 = -95.7 \pm$   
28.7 kJ mol<sup>-1</sup> and  $\Delta s_T^0 = -26.5 \pm 28.7$  J mol<sup>-1</sup> K<sup>-1</sup>.

The results here are in reasonable agreement with the fitted  
value using the defect model. The difference in  $\Delta h_T^0$  and  $\Delta s_T^0$   
may be attributed to the fact that ref 44 used  $[Ce^{3+}]_{\text{bulk}} =$   
0.0071 and for  $[Ce^{3+}]_{\text{surf}} = 0.36$  for the calculation, while the  
results from our model are based on the entire data set.  
Nevertheless, the difference is within the error bar.

## AUTHOR INFORMATION

### Corresponding Authors

\* (A.F.G.) E-mail: [ghoniem@mit.edu](mailto:ghoniem@mit.edu). Tel.: +1 617-253-2295.

\* (B.Y.) E-mail: [byildiz@mit.edu](mailto:byildiz@mit.edu). Tel.: +1 617-324-4009.

### Notes

The authors declare no competing financial interest.

## ACKNOWLEDGMENTS

This study is financially supported by a grant from British  
Petroleum (BP) and the King Abdullah University of Science  
and Technology (KAUST) Investigator Award.

## NOMENCLATURE

### Symbols

$a$	lattice constant, m	923
$a_i$	activity of species $i$	924
$C_i$	species molar concentration, mol m <sup>-3</sup>	925
$\tilde{C}_i$	species molar concentration on the surface, mol m <sup>-2</sup>	926
$D_i$	diffusion coefficient, m <sup>2</sup> s <sup>-1</sup>	927
$E$	activation energy, kJ mol <sup>-1</sup>	928
$F$	Faraday constant	929
$f$	difference between the measurements and the model predictions	930
$h$	molar enthalpy, kJ mol <sup>-1</sup>	931
$J_i$	diffusion flux from the bulk phase, mol m <sup>-2</sup>	932

933	$K_i$	equilibrium constant
		the rate coefficients for the forward and the backward
934	$k_{i,f}$ , $k_{i,b}$	reactions, $s^{-1}$
935	$m$	mass of sample, mg
936	$\dot{n}$	molar flow rate, $\text{mol s}^{-1}$
937	$p_i$	partial pressure of species $i$ , bar
938	$R$	gas constant
939	$\dot{R}_i$	production/consumption rate of species $i$ , $\text{mol m}^{-2} \text{s}^{-1}$
940	$r_p$	radius of ceria particle, m
941	$r_i$	reaction rate for reaction $i$ , $s^{-1}$
942	$S_R$	surface area of the spherical particle, $\text{m}^2$
943	$s_0$ , $s_1$	specific surface area of the fresh and aged samples, $\text{m}^2 \text{g}^{-1}$
944	$s$	molar enthalpy, $\text{J mol}^{-1} \text{K}^{-1}$
945	$T$	temperature, K
946	$V_R$	volume of the spherical particle, $\text{m}^3$
947	$\dot{V}$	volumetric flow rate, $\text{m}^3 \text{s}^{-1}$
948	$X_i$	species molar fraction
949	$z_i$	effective charge of species $i$

### 951 Greek Letters

952	$\gamma_i$	activity coefficient
953	$\Delta\delta$	bulk-phase nonstoichiometry change
954	$\tilde{\mu}_i$	electrochemical potential of species $i$ , $\text{J mol}^{-1}$
955	$\tilde{\mu}_i^*$	electrochemical potential with the diffusion of the defect $i$ , $\text{J mol}^{-1}$
956	$\tilde{\rho}_{\text{Ce}}$	molar density, $\text{mol m}^{-3}$
957	$\tilde{\rho}_{\text{Ce},s}$	surface molar density, $\text{mol m}^{-2}$
958	$\phi$	electrostatic potential, V
960	$\omega$	measured splitting rate, $\mu\text{mol g}^{-1}\text{s}^{-1}$

### 961 Acronyms

962	OC	oxygen carrier
963	QMS	quadrupole mass spectrometer
964	RCLWS	reactive chemical-looping water splitting
965	SC	space-charge region
966	SMR	steam methane reforming
968	TCWS	thermochemical water splitting

### 969 REFERENCES

- 970 (1) Hosseini, S. E.; Wahid, M. A. Hydrogen Production from  
971 Renewable and Sustainable Energy Resources: Promising Green  
972 Energy Carrier for Clean Development. *Renewable Sustainable Energy*  
973 *Rev.* **2016**, *57*, 850–866.
- 974 (2) Lemus, R. G.; Martínez Duart, J. M. Updated Hydrogen  
975 Production Costs and Parities for Conventional and Renewable  
976 Technologies. *Int. J. Hydrogen Energy* **2010**, *35*, 3929–3936.
- 977 (3) Ramsden, T.; Ruth, M.; Diakov, V.; Laffen, M.; Timbario, T.  
978 *Hydrogen Pathways: Updated Cost, Well-to-Wheels Energy Use, and*  
979 *Emissions for the Current Technology Status of Ten Hydrogen Production,*  
980 *Delivery, and Distribution Scenarios*, Technical Report NREL/TP-6A10-  
981 60528; National Renewable Energy Laboratory (NREL): Golden, CO,  
982 USA, 2013.
- 983 (4) Siegel, N. P.; Miller, J. E.; Ermanoski, I.; Diver, R. B.; Stechel, E.  
984 B. Factors Affecting the Efficiency of Solar Driven Metal Oxide  
985 Thermochemical Cycles. *Ind. Eng. Chem. Res.* **2013**, *52*, 3276–3286.
- 986 (5) Steinfeld, A. Solar Thermochemical Production of Hydrogen—  
987 Review. *Sol. Energy* **2005**, *78*, 603–615.
- 988 (6) Chueh, W. C.; Falter, C.; Abbott, M.; Scipio, D.; Furler, P.; Haile,  
989 S. M.; Steinfeld, A. High-flux Solar-driven Thermochemical Dissoci-  
990 ation of  $\text{CO}_2$  and  $\text{H}_2\text{O}$  using Nonstoichiometric Ceria. *Science* **2010**,  
991 *330*, 1797–1801.
- 992 (7) Hao, Y.; Yang, C.-K.; Haile, S. M. High-temperature Isothermal  
993 Chemical Cycling for Solar-driven Fuel Production. *Phys. Chem. Chem.*  
994 *Phys.* **2013**, *15*, 17084–17092.
- 995 (8) McDaniel, A. H.; Miller, E. C.; Arifin, D.; Ambrosini, A.; Coker,  
996 E. N.; O'Hayre, R.; Chueh, W. C.; Tong, J. Sr-and Mn-doped

- LaAlO<sub>3- $\delta$</sub>  for Solar Thermochemical H<sub>2</sub> and CO Production. *Energy* **997**  
*Environ. Sci.* **2013**, *6*, 2424–2428. 998
- (9) Gokon, N.; Suda, T.; Kodama, T. Thermochemical Reactivity of  
999 5–15 mol% Fe, Co, Ni, Mn-doped Cerium Oxides in Two-step Water-  
1000 splitting Cycle for Solar Hydrogen Production. *Thermochim. Acta*  
1001 **2015**, *617*, 179–190. 1002
- (10) Kaneko, H.; Miura, T.; Fuse, A.; Ishihara, H.; Taku, S.;  
1003 Fukuzumi, H.; Naganuma, Y.; Tamaura, Y. Rotary-type Solar Reactor  
1004 for Solar Hydrogen Production with Two-step Water Splitting  
1005 Process. *Energy Fuels* **2007**, *21*, 2287–2293. 1006
- (11) Meng, Q.-L.; Lee, C.-i.; Kaneko, H.; Tamaura, Y. Solar  
1007 Thermochemical Process for Hydrogen Production via Two-step  
1008 Water Splitting Cycle Based on Ce<sub>1-x</sub>Pr<sub>x</sub>O<sub>2- $\delta$</sub>  Redox Reaction.  
1009 *Thermochim. Acta* **2012**, *532*, 134–138. 1010
- (12) Le Gal, A.; Abanades, S. Dopant Incorporation in Ceria for  
1011 Enhanced Water-splitting Activity during Solar Thermochemical  
1012 Hydrogen Generation. *J. Phys. Chem. C* **2012**, *116*, 13516–13523. 1013
- (13) Pappacena, A.; Boaro, M.; Armelao, L.; Llorca, J.; Trovarelli, A.  
1014 Water Splitting Reaction on Ce<sub>0.15</sub>Zr<sub>0.85</sub>O<sub>2</sub> Driven by Surface  
1015 Heterogeneity. *Catal. Sci. Technol.* **2016**, *6*, 399–403. 1016
- (14) Le Gal, A.; Abanades, S. Catalytic Investigation of Ceria-zirconia  
1017 Solid Solutions for Solar Hydrogen Production. *Int. J. Hydrogen Energy*  
1018 **2011**, *36*, 4739–4748. 1019
- (15) Le Gal, A.; Abanades, S.; Bion, N.; Le Mercier, T.; Harlé, V.  
1020 Reactivity of Doped Ceria-Based Mixed Oxides for Solar Thermo-  
1021 chemical Hydrogen Generation via Two-Step Water-Splitting Cycles.  
1022 *Energy Fuels* **2013**, *27*, 6068–6078. 1023
- (16) Meng, Q.-L.; Lee, C.-i.; Ishihara, T.; Kaneko, H.; Tamaura, Y.  
1024 Reactivity of CeO<sub>2</sub>-based Ceramics for Solar Hydrogen Production via  
1025 a Two-step Water-splitting Cycle with Concentrated Solar Energy. *Int.*  
1026 *J. Hydrogen Energy* **2011**, *36*, 13435–13441. 1027
- (17) Kaneko, H.; Miura, T.; Ishihara, H.; Taku, S.; Yokoyama, T.;  
1028 Nakajima, H.; Tamaura, Y. Reactive Ceramics of CeO<sub>2</sub>–MO<sub>x</sub> (M=  
1029 Mn, Fe, Ni, Cu) for H<sub>2</sub> Generation by Two-step Water Splitting Using  
1030 Concentrated Solar Thermal Energy. *Energy* **2007**, *32*, 656–663. 1031
- (18) Lin, F.; Samson, V. A.; Wismer, A. O.; Grolimund, D.; Alxneit,  
1032 I.; Wokaun, A. Zn-modified Ceria as a Redox Material for  
1033 Thermochemical H<sub>2</sub>O and CO<sub>2</sub> Splitting: Effect of a Secondary  
1034 ZnO Phase on Its Thermochemical Activity. *CrystEngComm* **2016**, *18*,  
1035 2559–2569. 1036
- (19) Neises, M.; Roeb, M.; Schmücker, M.; Sattler, C.; Pitz-Paal, R.  
1037 Kinetic Investigations of the Hydrogen Production Step of a  
1038 Thermochemical Cycle Using Mixed Iron Oxides Coated on Ceramic  
1039 Substrates. *Int. J. Energy Res.* **2010**, *34*, 651–661. 1040
- (20) Charvin, P.; Abanades, S.; Flamant, G.; Lemort, F. Two-step  
1041 Water Splitting Thermochemical Cycle Based on Iron Oxide Redox  
1042 Pair for Solar Hydrogen Production. *Energy* **2007**, *32*, 1124–1133. 1043
- (21) Demont, A.; Abanades, S.; Beche, E. Investigation of Perovskite  
1044 Structures as Oxygen-Exchange Redox Materials for Hydrogen  
1045 Production from Thermochemical Two-Step Water-Splitting Cycles.  
1046 *J. Phys. Chem. C* **2014**, *118*, 12682–12692. 1047
- (22) Dey, S.; Naidu, B. S.; Govindaraj, A.; Rao, C. N. R. Noteworthy  
1048 Performance of La<sub>1-x</sub>Ca<sub>x</sub>MnO<sub>3</sub> Perovskites in Generating H<sub>2</sub> and CO  
1049 by the Thermochemical Splitting of H<sub>2</sub>O and CO<sub>2</sub>. *Phys. Chem. Chem.*  
1050 *Phys.* **2015**, *17*, 122–125. 1051
- (23) Zhao, Z.; Chen, T.; Ghoniem, A. F. Rotary Bed Reactor for  
1052 Chemical-Looping Combustion with Carbon Capture. Part I: Reactor  
1053 Design and Model Development. *Energy Fuels* **2013**, *27*, 327–343. 1054
- (24) Zhao, Z.; Iloje, C. O.; Chen, T.; Ghoniem, A. F. Design of a  
1055 Rotary Reactor for Chemical-Looping Combustion. Part I:  
1056 Fundamentals and Design Methodology. *Fuel* **2014**, *121*, 327–343. 1057
- (25) Zhao, Z.; Ghoniem, A. F. Design of a Rotary Reactor for  
1058 Chemical-looping Combustion. Part 2: Comparison of Copper-,  
1059 Nickel-, and Iron-based Oxygen Carriers. *Fuel* **2014**, *121*, 344–360. 1060
- (26) Zhao, Z.; Chen, T.; Ghoniem, A. F. Rotary Bed Reactor for  
1061 Chemical-Looping Combustion with Carbon Capture. Part 2: Base  
1062 Case and Sensitivity Analysis. *Energy Fuels* **2013**, *27*, 344–359. 1063

- 1064 (27) Iloeje, C.; Zhao, Z.; Ghoniem, A. F. Analysis of Thermally  
1065 Coupled Chemical Looping Combustion-based Power Plants with  
1066 Carbon Capture. *Int. J. Greenhouse Gas Control* **2015**, *35*, 56–70.
- 1067 (28) Iloeje, C.; Zhao, Z.; Ghoniem, A. F. Efficient Cycles for Carbon  
1068 Capture CLC Power Plants Based on Thermally Balanced Redox  
1069 Reactors. *Int. J. Greenhouse Gas Control* **2015**, *41*, 302–315.
- 1070 (29) Cho, W. C.; Seo, M. W.; Kim, S. D.; Kang, K. S.; Bae, K. K.;  
1071 Kim, C. H.; Jeong, S. U.; Park, C. S. Reactivity of Iron Oxide as an  
1072 Oxygen Carrier for Chemical-looping Hydrogen Production. *Int. J.*  
1073 *Hydrogen Energy* **2012**, *37*, 16852–16863.
- 1074 (30) Jin, G. T.; Ryu, H.-J.; Jo, S.-H.; Lee, S.-Y.; Son, S. R.; Kim, S. D.  
1075 Hydrogen Production in Fluidized Bed by Chemical-looping Cycle.  
1076 *Korean J. Chem. Eng.* **2007**, *24*, 542–546.
- 1077 (31) Sun, S.; Zhao, M.; Cai, L.; Zhang, S.; Zeng, D.; Xiao, R.  
1078 Performance of CeO<sub>2</sub>-Modified Iron-Based Oxygen Carrier in the  
1079 Chemical Looping Hydrogen Generation Process. *Energy Fuels* **2015**,  
1080 *29*, 7612–7621.
- 1081 (32) Chiron, F.-X.; Patience, G. S. Kinetics of Mixed Copper–iron  
1082 Based Oxygen Carriers for Hydrogen Production by Chemical  
1083 Looping Water Splitting. *Int. J. Hydrogen Energy* **2012**, *37*, 10526–  
1084 10538.
- 1085 (33) Son, S. R.; Go, K. S.; Kim, S. D. Thermogravimetric Analysis of  
1086 Copper Oxide for Chemical-Looping Hydrogen Generation. *Ind. Eng.*  
1087 *Chem. Res.* **2009**, *48*, 380–387.
- 1088 (34) Kang, K.-S.; Kim, C.-H.; Cho, W.-C.; Bae, K.-K.; Woo, S.-W.;  
1089 Park, C.-S. Reduction Characteristics of CuFe<sub>2</sub>O<sub>4</sub> and Fe<sub>3</sub>O<sub>4</sub> by  
1090 Methane; CuFe<sub>2</sub>O<sub>4</sub> as an Oxidant for Two-step Thermochemical  
1091 Methane Reforming. *Int. J. Hydrogen Energy* **2008**, *33*, 4560–4568.
- 1092 (35) Cha, K.-S.; Kim, H.-S.; Yoo, B.-K.; Lee, Y.-S.; Kang, K.-S.; Park,  
1093 C.-S.; Kim, Y.-H. Reaction Characteristics of Two-step Methane  
1094 Reforming over a Cu-ferrite/Ce–ZrO<sub>2</sub> Medium. *Int. J. Hydrogen*  
1095 *Energy* **2009**, *34*, 1801–1808.
- 1096 (36) Kang, K.-S.; Kim, C.-H.; Bae, K.-K.; Cho, W.-C.; Kim, W.-J.;  
1097 Kim, Y.-H.; Kim, S.-H.; Park, C.-S. Redox Cycling of CuFe<sub>2</sub>O<sub>4</sub>  
1098 Supported on ZrO<sub>2</sub> and CeO<sub>2</sub> for Two-step Methane Reforming/  
1099 Water Splitting. *Int. J. Hydrogen Energy* **2010**, *35*, 568–576.
- 1100 (37) Kodama, T.; Shimizu, T.; Satoh, T.; Nakata, M.; Shimizu, K.-I.  
1101 Stepwise Production of CO-rich Syngas and Hydrogen via Solar  
1102 Methane Reforming by Using a Ni (II)–ferrite Redox System. *Sol.*  
1103 *Energy* **2002**, *73*, 363–374.
- 1104 (38) Sim, A.; Cant, N. W.; Trimm, D. L. Ceria–zirconia Stabilised  
1105 Tungsten Oxides for the Production of Hydrogen by the Methane–  
1106 water Redox Cycle. *Int. J. Hydrogen Energy* **2010**, *35*, 8953–8961.
- 1107 (39) Otsuka, K.; Wang, Y.; Nakamura, M. Direct Conversion of  
1108 Methane to Synthesis Gas through Gas–solid Reaction using CeO<sub>2</sub>–  
1109 ZrO<sub>2</sub> Solid Solution at Moderate Temperature. *Appl. Catal., A* **1999**,  
1110 *183*, 317–324.
- 1111 (40) Zhu, X.; Wang, H.; Wei, Y.; Li, K.; Cheng, X. Hydrogen and  
1112 Syngas Production from Two-step Steam Reforming of Methane using  
1113 CeO<sub>2</sub> as Oxygen Carrier. *J. Nat. Gas Chem.* **2011**, *20*, 281–286.
- 1114 (41) Zhu, X.; Wang, H.; Wei, Y.; Li, K.; Cheng, X. Reaction  
1115 Characteristics of Chemical-looping Steam Methane Reforming over a  
1116 Ce–ZrO<sub>2</sub> Solid Solution Oxygen Carrier. *Mendeleev Commun.* **2011**,  
1117 *21*, 221–223.
- 1118 (42) Jeong, H. H.; Kwak, J. H.; Han, G. Y.; Yoon, K. J. Stepwise  
1119 Production of Syngas and Hydrogen through Methane Reforming and  
1120 Water Splitting by Using a Cerium Oxide Redox System. *Int. J.*  
1121 *Hydrogen Energy* **2011**, *36*, 15221–15230.
- 1122 (43) Zhu, X.; Wang, H.; Wei, Y.; Li, K.; Cheng, X. Hydrogen and  
1123 Syngas Production from Two-step Steam Reforming of Methane over  
1124 CeO<sub>2</sub>–Fe<sub>2</sub>O<sub>3</sub> Oxygen Carrier. *J. Rare Earths* **2010**, *28*, 907–913.
- 1125 (44) Chueh, W. C.; McDaniel, A. H.; Grass, M. E.; Hao, Y.; Jabeen,  
1126 N.; Liu, Z.; Haile, S. M.; McCarty, K. F.; Bluhm, H.; El Gabaly, F.  
1127 Highly Enhanced Concentration and Stability of Reactive Ce<sub>3+</sub> on  
1128 Doped CeO<sub>2</sub> Surface Revealed In Operando. *Chem. Mater.* **2012**, *24*,  
1129 1876–1882.
- 1130 (45) Feng, Z. A.; El Gabaly, F.; Ye, X.; Shen, Z.-X.; Chueh, W. C.  
1131 Fast Vacancy-Mediated Oxygen Ion Incorporation across the Ceria–  
1132 Gas Electrochemical Interface. *Nat. Commun.* **2014**, *5*, 4374.
- (46) Trovarelli, A. Catalytic Properties of Ceria and CeO<sub>2</sub>-containing  
Materials. *Catal. Rev.: Sci. Eng.* **1996**, *38*, 439–520. 1133
- (47) Mogensen, M.; Sammes, N. M.; Toppsett, G. A. Physical,  
Chemical and Electrochemical Properties of Pure and Doped Ceria. 1134  
*Solid State Ionics* **2000**, *129*, 63–94. 1135
- (48) Panlener, R.; Blumenthal, R.; Garnier, J. A Thermodynamic  
Study of Nonstoichiometric Cerium Dioxide. *J. Phys. Chem. Solids* 1136  
**1975**, *36*, 1213–1222. 1137
- (49) Tuller, H.; Nowick, A. Defect Structure and Electrical Properties  
of Nonstoichiometric CeO<sub>2</sub> Single Crystals. *J. Electrochem. Soc.* **1979**,  
1138 *126*, 209–217. 1139
- (50) Paier, J.; Penschke, C.; Sauer, J. Oxygen Defects and Surface  
Chemistry of Ceria: Quantum Chemical Studies Compared to  
Experiment. *Chem. Rev.* **2013**, *113*, 3949–3985. 1140
- (51) Marrocchelli, D.; Yildiz, B. First-principles Assessment of H<sub>2</sub>S  
and H<sub>2</sub>O Reaction Mechanisms and the Subsequent Hydrogen  
Absorption on the CeO<sub>2</sub> (111) Surface. *J. Phys. Chem. C* **2012**, *116*,  
1141 *2411–2424*. 1142
- (52) Hansen, H. A.; Wolverton, C. Kinetics and Thermodynamics of  
H<sub>2</sub>O Dissociation on Reduced CeO<sub>2</sub> (111). *J. Phys. Chem. C* **2014**,  
1143 *118*, 27402–27414. 1144
- (53) Watkins, M. B.; Foster, A. S.; Shluger, A. L. Hydrogen Cycle on  
CeO<sub>2</sub> (111) Surfaces: Density Functional Theory Calculations. *J. Phys.*  
1145 *Chem. C* **2007**, *111*, 15337–15341. 1146
- (54) Zhang, C.; et al. Measuring Fundamental Properties in  
Operating Solid Oxide Electrochemical Cells by Using in situ X-ray  
Photoelectron Spectroscopy. *Nat. Mater.* **2010**, *9*, 944–949. 1147
- (55) DeCaluwe, S. C.; Grass, M. E.; Zhang, C.; Gabaly, F. E.; Bluhm,  
H.; Liu, Z.; Jackson, G. S.; McDaniel, A. H.; McCarty, K. F.; Farrow, R.  
1148 *L.; Linne, M. A.; Hussain, Z.; Eichhorn, B. W. In Situ Characterization*  
1149 *of Ceria Oxidation States in High-Temperature Electrochemical Cells*  
1150 *with Ambient Pressure XPS. J. Phys. Chem. C* **2010**, *114*, 19853–  
1151 19861. 1152
- (56) Feng, Z. A.; Machala, M. L.; Chueh, W. C. Surface  
Electrochemistry of CO<sub>2</sub> Reduction and CO Oxidation on Sm-  
1153 *doped CeO<sub>2</sub>: Coupling between Ce<sub>3+</sub> and Carbonate Adsorbates.*  
1154 *J. Phys. Chem. Phys.* **2015**, *17*, 12273–12281. 1155
- (57) Ackermann, S.; Scheffe, J. R.; Steinfeld, A. Diffusion of Oxygen  
in Ceria at Elevated Temperatures and Its Application to H<sub>2</sub>O/CO<sub>2</sub>  
1156 *Splitting Thermochemical Redox Cycles. J. Phys. Chem. C* **2014**, *118*,  
1157 *5216–5225*. 1158
- (58) Al-Madfaa, H. A.; Khader, M. M. Reduction Kinetics of Ceria  
Surface by Hydrogen. *Mater. Chem. Phys.* **2004**, *86*, 180–188. 1159
- (59) Bulfin, B.; Lowe, A. J.; Keogh, K. A.; Murphy, B. E.; Lübben, O.;  
Krasnikov, S. A.; Shvets, I. V. Analytical Model of CeO<sub>2</sub> Oxidation and  
1160 *Reduction. J. Phys. Chem. C* **2013**, *117*, 24129–24137. 1161
- (60) Knoblauch, N.; Dorrer, L.; Fielitz, P.; Schmucker, M.;  
Borchardt, G. Surface Controlled Reduction Kinetics of Nominally  
1162 *Undoped Polycrystalline CeO<sub>2</sub>. Phys. Chem. Chem. Phys.* **2015**, *17*,  
1163 *5849–5860*. 1164
- (61) Chen, T. Experimental Characterization and Chemical Kinetics  
Study of Chemical Looping Combustion, Master's Thesis; Massachu-  
1165 *setts Institute of Technology: Cambridge, MA, USA, 2014.* 1166
- (62) Maier, J. *Physical Chemistry of Ionic Materials: Ions and Electrons*  
1167 *in Solids; John Wiley & Sons: Chichester, U.K., 2004.* 1168
- (63) Stan, M.; Zhu, Y. T.; Jiang, H.; Butt, D. P. Kinetics of Oxygen  
Removal from Ceria. *J. Appl. Phys.* **2004**, *95*, 3358–3361. 1169
- (64) Lagarias, J. C.; Reeds, J. A.; Wright, M. H.; Wright, P. E.  
Convergence Properties of the Nelder-Mead Simplex Method in Low  
1170 *Dimensions. SIAM Journal on optimization* **1998**, *9*, 112–147. 1171